Three-dimensional data-tracking simulations of sprinting using a direct collocation optimal control approach

Nicos Haralabidis [Corresp., 1, 2], Gil Serrancolí [3], Steffi Colyer [1, 2], Ian Bezodis [4], Aki Salo [1, 2, 5], Dario Cazzola [1, 2]

[1] Department for Health, University of Bath, Bath, United Kingdom

[2] CAMERA-Centre for the Analysis of Motion, Entertainment Research and Applications, Bath, United Kingdom

[3] Department of Mechanical Engineering, Universitat Politècnica de Catalunya, Barcelona, Spain

[4] Cardiff School of Sport and Health Sciences, Cardiff Metropolitan University, Cardiff, United Kingdom

[5] KIHU Research Institute for Olympic Sports, Jyväskylä, Finland

Corresponding Author: Nicos Haralabidis
Email address: nh546@bath.ac.uk

Biomechanical simulation and modelling approaches have the possibility to make a meaningful impact within applied sports settings, such as sprinting. However, for this to be realised, such approaches must first undergo a thorough quantitative evaluation against experimental data. We developed a musculoskeletal modelling and simulation framework for sprinting, with the objective to evaluate its ability to reproduce experimental kinematics and kinetics data for different sprinting phases. This was achieved by performing a series of data-tracking calibration (individual and simultaneous) and validation simulations, that also featured the generation of dynamically consistent simulated outputs and the determination of foot-ground contact model parameters. The simulated values from the calibration simulations were found to be in close agreement with the corresponding experimental data, particularly for the kinematics (average root mean squared differences (RMSDs) less than 1.0° and 0.2 cm for the rotational and translational kinematics, respectively) and ground reaction force (GRF) (highest average percentage RMSD of 8.1%). Minimal differences in tracking performance were observed when concurrently determining the foot-ground contact model parameters from each of the individual or simultaneous calibration simulations. The validation simulation yielded results that were comparable (RMSDs less than 1.0° and 0.3 cm for the rotational and translational kinematics, respectively) to those obtained from the calibration simulations. This study demonstrated the suitability of the proposed framework for performing future predictive simulations of sprinting, and gives confidence in its use to assess the cause-effect relationships of technique modification in relation to performance. Furthermore, this is the first study to provide dynamically consistent three-dimensional muscle-driven simulations of sprinting across different phases.

1 # Three-dimensional data-tracking simulations of sprinting
2 # using a direct collocation optimal control approach
3

5 Nicos Haralabidis[1,2], Gil Serrancolí[3], Steffi L. Colyer[1,2], Ian N. Bezodis[4], Aki I.T. Salo[5,1,2], Dario
6 Cazzola[1,2]
7
8 [1] Department for Health, University of Bath, UK
9 [2] CAMERA-Centre for the Analysis of Motion, Entertainment Research and Applications,
10 University of Bath, UK
11 [3] Department of Mechanical Engineering, Universitat Politècnica de Catalunya, Barcelona, Spain
12 [4] Cardiff School of Sport and Health Sciences, Cardiff Metropolitan University, Cardiff, UK
13 [5] KIHU Research Institute for Olympic Sports, Jyväskylä, Finland
14

16 Corresponding Author:
17 Nicos Haralabidis[1,2]
18 Claverton Down, Bath, Bath and North East Somerset, BA2 7AY, UK
19 Email address: n.haralabidis@bath.ac.uk

21
22
23
24
25
26
27
28
29
30
31
32
33
34
35
36
37
38
39
40

Abstract

Biomechanical simulation and modelling approaches have the possibility to make a meaningful impact within applied sports settings, such as sprinting. However, for this to be realised, such approaches must first undergo a thorough quantitative evaluation against experimental data. We developed a musculoskeletal modelling and simulation framework for sprinting, with the objective to evaluate its ability to reproduce experimental kinematics and kinetics data for different sprinting phases. This was achieved by performing a series of data-tracking calibration (individual and simultaneous) and validation simulations, that also featured the generation of dynamically consistent simulated outputs and the determination of foot-ground contact model parameters. The simulated values from the calibration simulations were found to be in close agreement with the corresponding experimental data, particularly for the kinematics (average root mean squared differences (RMSDs) less than 1.0° and 0.2 cm for the rotational and translational kinematics, respectively) and ground reaction force (GRF) (highest average percentage RMSD of 8.1%). Minimal differences in tracking performance were observed when concurrently determining the foot-ground contact model parameters from each of the individual or simultaneous calibration simulations. The validation simulation yielded results that were comparable (RMSDs less than 1.0° and 0.3 cm for the rotational and translational kinematics, respectively) to those obtained from the calibration simulations. This study demonstrated the suitability of the proposed framework for performing future predictive simulations of sprinting, and gives confidence in its use to assess the cause-effect relationships of technique modification in relation to performance. Furthermore, this is the first study to provide dynamically consistent three-dimensional muscle-driven simulations of sprinting across different phases.

Introduction

Sprinting is the fastest mode of human bipedal locomotion, and the short distance events (60-400 m) in modern athletics provide a means of assessing the limits of human sprinting performance. The objective for athletes competing within these events is to cover the set distance in the shortest possible time, and often the winning margin is hundredths of a second at the highest levels of competition. Coaches and athletes are therefore continually striving for improvements in technique which can enhance overall performance by such fine margins. Sprinting also plays an important role within team-based sports. For instance, sprinting has been shown to be pivotal in creating goal scoring opportunities within soccer (Faude et al., 2012). Thus, the insights from further understanding sprinting technique and performance can have far reaching applications, as they can also be transferred to benefit performance in other sports.

Most studies to date have advanced the knowledge of how to improve sprinting performance by assessing the ground reaction force (GRF) (Colyer et al., 2018; Morin et al., 2011), joint kinematics and kinetics (Bezodis et al., 2008; Schache et al., 2019; Smith et al., 2014), and spatiotemporal parameters (Hunter et al., 2004; Salo et al., 2011). The studies focusing on joint kinetics (net joint moments, power, and work) potentially bear the most significance, as they can explain the causes of motion. However, the net joint moments calculated from inverse dynamics analyses (IDA) are known to be impacted by several factors (Derrick et al., 2020) (e.g., filtering and soft-tissue artefact), and necessitate fictitious residual forces and moments to be applied at the model's root segment (e.g., pelvis) due to dynamic inconsistencies. These residuals are further exacerbated during explosive tasks, such as sprinting, where experimental errors and modelling assumptions are likely to become more critical. Methods such as the residual reduction algorithm (RRA) within OpenSim (Delp et al., 2007) and optimal control approaches (Lin and Pandy, 2017; Meyer et al., 2016; Pallarès-López et al., 2019) have been introduced to compensate for the residuals, although they have not seen widespread adoption within the sports biomechanics literature. Furthermore, within the sports biomechanics literature these residuals are typically neglected, raising questions on the errors in IDA and the validity of the corresponding findings.

A further limitation within the current body of sprinting literature is that most studies have focused on identifying key aspects of technique from group level analyses. It is possible that the technique based findings from group level analyses can be transferred to benefit the performance levels of elite athletes. However, individualised technique modifications are more likely to be necessary for elite athletes to further improve their performance levels by the sought-after small margins. Furthermore, the existing literature provides various technique related factors associated with improved sprinting performance, as opposed to how specific technique modifications influence sprinting performance. Predictive computer simulation and modelling approaches within sports biomechanics can be used to overcome the aforementioned limitations,

119 as they can be used to identify optimum technique on an individualised basis, explore cause-
120 effect relationships, and assess 'what-if' scenarios (Neptune, 2000).

121

122 Recently, there has been a noticeable increase in the number of modelling and simulation studies
123 within sports biomechanics adopting an optimal control theory approach (Jansen and McPhee,
124 2020; Lin and Pandy, 2017; Porsa et al., 2016), also specifically within sprinting (Celik and
125 Piazza, 2013; Schultz and Mombaur, 2010). Celik and Piazza (2013) found that their optimised
126 solution of sprinting demonstrated several salient features that have been observed
127 experimentally (e.g., forward trunk lean during early acceleration), although their model lacked a
128 sufficient representation of the lower-limbs to adequately characterise their actions. Conversely,
129 Schultz and Mombaur (2010) developed a three-dimensional model, and used it in an exploratory
130 sense to determine the feasibility of performing predictive sprinting simulations. However, a
131 limitation common to both of these studies is that they did not explicitly evaluate their outputs
132 against experimental data.

133

134 The evaluation of a modelling and simulation framework is needed to ensure that it is fit for its
135 purposes and produces realistic results (Yeadon and Challis, 1994). Furthermore, within applied
136 sports contexts the evaluation step is necessary to ensure that the results from predictive
137 simulations can be transferred with confidence to drive real world changes. To conduct the
138 evaluation step, data-tracking simulations using optimal control theory can be performed
139 (Umberger and Miller, 2017), as they provide the opportunity to quantitatively determine how a
140 modelling and simulation framework performs at reproducing experimental data. In addition, a
141 major benefit of optimal control based data-tracking simulations is that they provide an elegant
142 approach to improve the dynamic consistency of a simulation by either minimising or
143 constraining the residuals, particularly when used with the direct collocation method (Lin and
144 Pandy, 2017; Meyer et al., 2016; Pallarès-López et al., 2019). To date, however, no study has
145 attempted to use this approach within a highly demanding sporting movement, such as sprinting.

146

147 Lastly, predictive simulations of sprinting necessitate a means of modelling the foot-ground
148 interaction. One popular approach relies on distributing a finite set of contact elements across the
149 surface of a foot and using a compliant foot-ground contact model to calculate the contact forces
150 at each element (Dorschky et al., 2019; Falisse et al., 2019a; Falisse et al., 2019b; Gilchrist and
151 Winter, 1996; Lin and Pandy, 2017; Serrancolí et al., 2019). The difficulty with using this
152 approach is determining the foot-ground contact model parameters. Previous studies have
153 obtained the foot-ground contact model parameters by fitting their model to mechanical testing
154 data (Dorschky et al., 2019; Miller and Hamill, 2015), thus the values of the parameters can be
155 used by further studies. However, the use of previously published foot-ground contact model
156 parameter values can be problematic due to the differences in the formulations and constitutive
157 laws between compliant foot-ground contact models. It is also possible to determine the values
158 of the foot-ground contact model parameters by manually tuning them (Gilchrist and Winter,

159   1996), although this approach can be challenging to implement due to the nonlinear interactions
160   of the parameters. An alternative approach is to perform data-tracking simulations, as they
161   enable the foot-ground contact model parameter values to be determined in addition to the
162   evaluation of a modelling and simulation framework (Falisse et al., 2019a; Serrancolí et al.,
163   2019). When using the latter approach, care must be taken to ensure that the parameters obtained
164   are not unrealistic and overfit, particularly if they are determined from tracking a single trial.
165   Consequently, further independent data-tracking simulations using the obtained foot-ground
166   contact model parameters must be performed to ensure that they lead to simulated outputs that
167   closely resemble the experimental data, and to provide confidence for their use within predictive
168   simulations.
169
170   The main aims of this study were to develop a musculoskeletal modelling and simulation
171   framework for sprinting, and to evaluate its capability of reproducing experimental data (GRF,
172   kinematics, kinetics, and electromyograms – EMGs) by performing data-tracking simulations.
173   The secondary aims of this study were to improve the dynamic consistency of the simulated
174   outputs by enforcing the residuals to be zero, thus further highlighting the advantages of the
175   approach used, and to identify foot-ground contact model parameters such that they can be used
176   within future predictive simulations of sprinting.
177

Materials & Methods

179
Experimental Data Collection
181   An international-level male sprinter (age: 24 years; height: 1.79 m; mass: 72.2 kg; 100 m PB:
182   10.33 s; 200 m PB: 20.27 s) provided written informed consent to participate in the current
183   study. Ethical approval for this study was obtained from the University of Bath's Research
184   Ethics Approval Committee for Health (EP 17/18 238). The data collection took place at the
185   National Indoor Athletics Centre in Cardiff, UK (Fig. 1). The protocol required the athlete to
186   perform a series of maximal sprinting trials whilst GRF, three-dimensional marker trajectories
187   and EMGs were recorded.
188
189   Five force plates (× 4 type: 9287CA and × 1 type 9282BA, Kistler, Switzerland) were used to
190   collect GRF at a sampling frequency of 2000 Hz. Three-dimensional marker trajectories were
191   recorded using a 15-camera motion capture system (Qualisys AB, Sweden) sampling at 250 Hz.
192   The motion capture system was positioned on either side of the track segment which enclosed
193   the force plates. Forty-nine retro-reflective markers were attached to the surface of the athlete's
194   skin and shoes using double-sided adhesive and medical tapes (Fig. 1). Eight acrylic marker
195   clusters were also attached to the athlete using double-sided adhesive tape and medical bandages.
196   Six wireless surface electrodes (Trigno Avanti, Delsys Inc., Boston, MA, USA) sampling at 2000
197   Hz with a 20-450 Hz bandwidth were used to record EMGs from the following right lower-limb
198   muscles of the athlete: gluteus maximus (GMAX), biceps femoris (BF), medial gastrocnemius

199 (GASTM), tensor fasciae latae (TFL), vastus medialis (VM) and soleus (SOL). The skin
200 preparation and placement of the electrodes was in accordance with previously published
201 guidelines (Hermens et al., 2000).
202
203 *[Place Figure 1 about here]*
204 **Figure 1. Experimental data collection setup (A), and placement of retro-reflective markers, acrylic clusters, and**
205 **EMG electrodes (B-C).**
206 *The force plates setup provided a 4.5 m segment of the track to capture GRF, and this permitted GRF data from a*
207 *minimum of two successive steps to be captured for each trial. The calibrated motion capture volume covered*
208 *approximately 9.5 (length) × 1.5 (width) × 2 (height) m³.*
209
210 The data collection commenced with a standing static trial of the athlete being captured. The
211 athlete then performed two successful maximal effort sprints over three distances (0-10, 0-30 and
212 0-60 m) following the completion of a self-led warm up. The chosen distances covered the three
213 conventional phases (early acceleration, mid-acceleration and maximum velocity) of short
214 distance sprinting events. Different starting positions, relative to the first force plate, were used
215 to enable the sprinter to contact the force plates between 0-5, 10-15 and 45-50 m for each of the
216 distances. A trial was deemed successful if the athlete's entire foot landed within the boundaries
217 of a single force plate whilst not noticeably altering their step. A rest period of up to 10 minutes
218 between each sprint was given to the athlete. Each sprint was initiated by standard '*on your*
219 *marks*' and '*set*' commands by a member of the research team. The researcher then pressed a
220 trigger button that provided an auditory sound signal through a sounder device (Wee Beastie Ltd,
221 UK), and this also triggered the synchronous acquisition of GRF, three-dimensional marker
222 trajectories and EMGs through Qualisys Track Manager (version 2018.1, Qualisys AB, Sweden).
223
224 ***Model***
225 We started with a generic three-dimensional full-body musculoskeletal OpenSim model (Hamner
226 et al., 2010) (Fig. 2) that had been previously used for applications in sprinting (Dorn et al.,
227 2012; Lai et al., 2016). The original model represented the human skeleton as a multibody
228 system comprising 20 rigid segments and 29 degrees-of-freedom (DOFs). We added DOFs for
229 subtalar inversion-eversion, metatarsophalangeal (MTP) dorsiflexion-plantarflexion, and wrist
230 flexion-extension and adduction-abduction. The configuration of the modified model was
231 uniquely described by a set of generalised coordinates $q \in \mathbb{R}^{37}$, with each DOF being
232 represented by a generalised coordinate. The modified model's 37 DOFs were as follows: 6
233 DOFs ground-to-pelvis joint, 3 DOFs hip joints, 1 DOF knee joints, 1 DOF ankle joints, 1 DOF
234 subtalar joints, 1 DOF MTP joints, 3 DOFs back joint, 3 DOFs shoulder joints, 2 DOFs elbow
235 joints and 2 DOFs wrist joints.
236
237 *[Place Figure 2 about here]*
238 **Figure 2. Three-dimensional musculoskeletal model (Hamner et al., 2010) used in the current study.**
239 *The same model was used to determine experimental kinematics and kinetics from inverse kinematics and dynamics*
240 *analyses, respectively, and perform data-tracking simulations. The virtual model markers are denoted by pink spheres.*

241

242 The generic modified model was linearly scaled to match the anthropometric and inertial
243 characteristics of the athlete by using a measurement-based approach within OpenSim. Scaling
244 factors for each segment were calculated using the relative distances between markers placed
245 over anatomical landmarks recorded in the static trial and corresponding virtual markers which
246 were placed on the modified generic model. A combination of uniform and non-uniform scaling
247 factors were used to scale the properties of each segment, and the lower- and upper-limbs were
248 scaled to maintain bilateral symmetry.

249

250 The upper-limbs were actuated by 14 joint actuators whose limits were set based upon the IDA
251 results. The lower-limbs and trunk were actuated by 92 Hill-type muscle-tendon units (MTUs),
252 and we used the dimensionless characteristic equations presented by De Groote et al. (2016) to
253 describe the active and passive (series and parallel) components of force generation for each
254 MTU. Five parameters are used to scale the dimensionless characteristic equations of Hill-type
255 models for a specific MTU: pennation angle at optimum fibre length, optimum fibre length,
256 tendon slack length, maximum shortening velocity and maximum isometric force. In our case we
257 used the pennation angle at optimum fibre length parameters reported in the generic model,
258 whilst we used the optimum fibre length and tendon slack length parameters obtained following
259 the scaling of our model. The scaling procedure updated those parameters while preserving the
260 ratio between them from the generic model. We set the maximum shortening velocity parameter
261 of all the MTUs to be 12 optimal fibre lengths per second based upon an *in vivo* estimate of the
262 maximum shortening velocity of human muscle (De Ruiter et al., 2000). The maximum isometric
263 force parameters were set to be two times greater than those reported within the generic model,
264 and this enabled the MTUs of the lower-limbs DOFs, except the MTP DOFs, to exert net
265 moments that more closely reflected the training status of our athlete. For example, the four
266 MTUs responsible for extension of the knee DOF had the capacity to exert an isometric net
267 moment that was approximately 18% greater than reported by Erskine et al. (2011) for a group of
268 untrained individuals following 9 weeks of resistance training.We also included reserve actuators
269 for each of the lower-limb and trunk DOFs. The upper limits of the reserve actuators for the
270 MTP DOFs and the remaining lower-limb and trunk DOFs were set to 40 and 10 Nm,
271 respectively. The reserve actuators for the MTP DOFs were set with a higher upper limit such
272 that together with the four MTUs spanning each of the MTP DOFs they had the capacity to
273 produce net MTP moments that were in a similar range to those reported from isometric
274 dynamometry testing (Goldmann et al., 2013). To account for the behaviour of the athlete's
275 sprinting spikes and the passive structures surrounding the MTP DOFs we included a simple
276 linear rotational spring. The stiffness of the rotational spring was set to 65 Nm/rad by combining
277 the rotational stiffness of sprinting spikes/sports shoes (Oh and Park, 2017; Toon et al., 2006)
278 with the rotational stiffness used previously for representing the passive structures surrounding
279 the MTP DOFs (Sasaki et al., 2009).

280

281   Polynomials were used to describe the lengths, velocities and moment arms of the MTUs as
282   functions of the model's generalised coordinates and velocities (Falisse et al., 2019a). The
283   coefficients of the polynomials were determined by fitting them to the lengths and moment arms
284   of the scaled model's MTUs, which were obtained by performing a Muscle Analysis within
285   OpenSim for a wide range of generalised coordinates values. We opted to describe the lengths,
286   velocities and moment arms of the MTUs with differentiable and continuous polynomial
287   functions as they are ideally suited to the gradient-based optimal control approach we used.
288
289   The aerodynamic drag force within sprinting is known to have an influence on overall
290   performance (Quinn, 2003), even when analysing performance across multiple steps with zero
291   wind velocity (Colyer et al., 2018). To account for the aerodynamic drag force we used the
292   approach presented by Samozino et al. (2016), and for this study we assumed that the wind
293   velocity was zero as the experimental data collection took place in an indoor athletics centre. The
294   aerodynamic drag force was applied to the pelvis segment, specifically at the model's centre of
295   mass position expressed in the local frame of the pelvis segment. We opted to apply the
296   aerodynamic drag force to the pelvis segment as this segment was the closest to the model's
297   centre of mass position when visualised within the OpenSim graphical user interface for the trials
298   processed.
299

300   ***Data Processing & Analysis***
301   An open-source MATLAB toolbox (https://simtk.org/projects/matlab_tools) was used to convert
302   the raw data into the file formats compatible with OpenSim (version 3.3, Stanford University,
303   CA,USA) (Delp et al., 2007). For the purposes of this study we used experimental data that
304   spanned an arbitrary right foot stance phase alongside portions of the flight phases prior to
305   touchdown and after take-off from the first early acceleration and mid-acceleration phase trials
306   and from both the maximum velocity phase trials. Touchdown and take-off were determined
307   using a 20 N vertical GRF threshold. The analysed flight phases were identified by searching
308   within the vertical GRF signal 50 frames backwards and forwards from touchdown and take-off,
309   respectively, to then identify the frames which most closely coincided with the sampling
310   intervals of the motion capture system.
311

312   Global pelvis and relative joint kinematics for each trial were determined by performing inverse
313   kinematics analyses within OpenSim from the recorded marker trajectories. The kinematics and
314   GRF were filtered using a common 20 Hz fourth-order low-pass Butterworth filter. The cut-off
315   frequency was determined by performing a residual analysis on the kinematics obtained from the
316   inverse kinematics analyses (Winter, 2009). The filtered kinematics were also fitted using B-
317   splines to enable velocities and accelerations to be determined. Net joint moments and pelvis
318   residuals were calculated for each trial by performing IDA using the OpenSim C++ application
319   programming interface. The splined kinematics, net joint moments and filtered GRF served as
320   the experimental data to be tracked within the data-tracking simulations.
321

322   The EMGs from each trial were full-wave rectified and filtered at 20 Hz using a fourth-order
323   low-pass Butterworth filter. We selected the cut-off frequency based on previous studies which
324   assessed EMGs during running and sprinting (Santuz et al., 2020; Yong et al., 2014). Each
325   filtered EMG was normalised to the maximum filtered amplitude of the respective EMG from
326   within all the trials processed. Following the collection of the mid-acceleration and maximum
327   velocity phase trials we noticed that the TFL and SOL electrodes, respectively, became detached
328   from the surface of the athlete's skin, consequently we excluded the TFL and SOL EMG from
329   those trials during data processing and further analysis.
330
331   ***Optimal Control Problem Formulation***
332   The data-tracking simulations (calibration and validation) were formulated as optimal control
333   problems (OCPs). The objective of the data-tracking simulations was to determine the state x
334   and control u variables (plus the foot-ground contact model parameters p for the calibration
335   simulations), that resulted in tracking the experimental data as closely as possible, while
336   satisfying our model's constraints.
337
338   The skeletal dynamics of our musculoskeletal model (Fig. 2) were described by a collection of
339   37 coupled second-order nonlinear differential equations. The contraction and activation
340   dynamics of each MTU were described by two first-order nonlinear differential equations (De
341   Groote et al., 2016; Zajac, 1989). Four state variables ($x = [q\ v\ F_T\ a]$, where q and v are the
342   scaled musculoskeletal model's generalised coordinates and velocities, respectively, and F_T and
343   a are the MTU normalised tendon forces and activations, respectively) were selected to enable
344   the skeletal, contraction and activation dynamics to be represented as a system of first-order
345   differential equations. We also included control variables for the upper-limb joint actuators u_{UL}
346   and the reserve actuators u_{RES} that defined the instantaneous moment those actuators could
347   produce.
348
349   We formulated the differential equations governing skeletal and contraction dynamics implicitly
350   (Falisse et al., 2019a) by introducing additional control variables for the time derivatives of the
351   generalised velocities $u_{\dot{v}}$ and normalised tendon forces $u_{\dot{F}_T}$. The implicit formulation led to
352   enforcing the first-order skeletal and contraction dynamics with simple constraints, and
353   additional nonlinear equality path constraints were used to ensure the skeletal and contraction
354   dynamics equations were enforced. Two sets of equality path constraints were used to enforce
355   the skeletal dynamics equations of our model's 37 DOFs. The first set enforced that the pelvis
356   residuals (moments and forces at the 6 pelvis DOFs) obtained from evaluating the skeletal
357   dynamics equations were zero. The second set enforced that the net joint moments (moments at
358   the 31 relative DOFs) obtained from evaluating the skeletal dynamics equations matched with
359   those obtained from the actuators. The inclusion of the control variables for the upper-limb
360   actuators was not mandatory since we used idealised upper-limb actuators together with an

361 implicit skeletal dynamics formulation. For the contraction dynamics equations we imposed
362 equality path constraints to enforce the Hill-equilibrium condition (the normalised tendon force
363 matched the projected normalised muscle force).

364

365 The differential equation describing activation dynamics was also formulated implicitly using the
366 approach presented by De Groote et al. (2009), and we introduced additional control variables
367 for the time derivatives of the activations $\boldsymbol{u}_{\dot{a}}$. This again led to enforcing the first-order

368 activation dynamics with simple constraints, and we enforced the activation dynamics equations
369 by imposing two sets of linear inequality path constraints. These constraints can be derived from
370 the original differential equation describing activation dynamics by using the upper and lower
371 bounds of the excitations, which are often used as control variables. By formulating the
372 activation dynamics in this manner we avoided the need to include excitations as control
373 variables, and the resulting path constraints possessed favourable optimisation properties as they
374 were linear.

375

376 For the purposes of modelling foot-ground interaction we attached four and two contact spheres
377 to our model's right rearfoot and forefoot segments, respectively. The GRF generated by each of
378 the contact spheres was based on a smooth foot-ground contact model (Serrancolí et al., 2019).
379 The smooth foot-ground contact model was designed to be compatible with gradient-based
380 optimal control approaches and is an approximation of a previously published foot-ground
381 contact model (Sherman et al., 2011). The equations used to calculate the normal and friction
382 forces for the smooth foot-ground contact model can be accessed online at
383 https://simbody.github.io/3.7.0/classSimTK_1_1SmoothSphereHalfSpaceForce.html. The
384 position of each contact sphere relative to the segment it was attached to, and the stiffness and
385 damping coefficients common to all the contact spheres were treated as parameters $\boldsymbol{p}$ to be
386 determined from the data-tracking calibration simulations. A constraint was added to ensure that
387 the contact spheres lie on a horizontal plane when the ankle, subtalar and MTP DOFs were
388 neutral. We used the default parameters for the constants responsible for smoothing the
389 penetration and penetration rate terms, and the constant that enforces the derivative of the
390 penetration term to be non-zero. For each contact sphere, the static, dynamic and viscous
391 coefficients of friction were set to 0.95, 0.3 and 0.3, respectively, and the transition velocity and
392 radius were set to 0.001 m/s and 0.02 m, respectively. We also introduced GRF control variables
393 $\boldsymbol{u}_{GRF}$ for each of the contact spheres, similarly to Serrancolí et al. (2019). GRF control variables
394 were introduced to improve the conditioning of the objective function, as the GRF computed
395 from the contact model is susceptible to large changes with only minor changes in the
396 musculoskeletal model's state variables, which can lead to convergence issues. Equality path
397 constraints were included to ensure the GRF from both the control variables and the contact
398 model matched at the optimal solution.

399

400 The objective function J consisted of three terms: a data-tracking term $J_{tracking}$ that minimised
401 the squared errors between the experimental and simulated kinematics, GRF and net joint
402 moments, an effort term J_{effort} that minimised the squared activations, and a control variables
403 term $J_{control}$ that minimised the squared reserve actuators control variables and those control
404 variables introduced due to the use of the implicit differential equations:

405

$$J = J_{tracking} + J_{effort} + J_{control} \quad \#(1)$$

406

407

$$J_{tracking} = w_1 \sum_{j=1}^{37} \int_{t_0}^{t_f} \left(\frac{q_j^{EXP} - q_j^{SIM}}{range(q_j^{EXP})} \right)^2 dt + w_1 \sum_{n=1}^{6} \int_{t_0}^{t_f} \left(\frac{GRF_n^{EXP} - u_{GRF_n}^{SIM}}{range(GRF_n^{EXP})} \right)^2 dt$$

408

$$+ w_2 \sum_{k=1}^{29} \int_{t_0}^{t_f} \left(\frac{\tau_k^{EXP} - \tau_k^{SIM}}{range(\tau_k^{EXP})} \right)^2 dt \quad \#(2)$$

409

$$J_{effort} = w_3 \sum_{i=1}^{92} \int_{t_0}^{t_f} \left(\frac{F_i^{max} a_i^{SIM^2}}{\sum_{i=1}^{92} F_i^{max}} \right) dt \quad \#(3)$$

410

411

$$J_{control} = w_4 \sum_{m=1}^{17} \int_{t_0}^{t_f} \left(\frac{u_{res_m}^{SIM}}{bound(u_{res_m}^{SIM})} \right)^2 dt + w_5 \sum_{j=1}^{37} \int_{t_0}^{t_f} \left(\frac{u_{\dot{v}_j}^{SIM}}{range(\ddot{q}_j^{EXP})} \right)^2 dt$$

412

$$+ w_5 \sum_{i=1}^{92} \int_{t_0}^{t_f} \left(\frac{u_{\dot{F}_{T_i}}^{SIM}}{bound(u_{\dot{F}_{T_i}}^{SIM})} \right)^2 dt + w_5 \sum_{i=1}^{92} \int_{t_0}^{t_f} \left(\frac{u_{\dot{a}_i}^{SIM}}{bound(u_{\dot{a}_i}^{SIM})} \right)^2 dt \quad \#(4)$$

413

414 where the superscripts EXP and SIM denote experimental and simulated variables, respectively,
415 t_0 and t_f denote the initial and final times, respectively, of the experimental data from the trial
416 being tracked, τ_k are the net joint moments, F_i^{max} are the MTU maximal isometric force
417 parameters, and w_i are the weighting factors whose values were set based upon the importance of
418 the term being tracked or minimised ($\mathbf{w} = [0.1\ 0.01\ 0.001\ 0.01\ 0.0001]$).

419

420 The objective function weighting factors were chosen heuristically, and we placed a greater
421 emphasis on tracking the variables we believed were closer to the ground-truth (kinematics and
422 GRF) whilst ensuring we obtained dynamically consistent solutions. To achieve those objectives

423   it was necessary to place a lower weighting on the tracking of the net joint moments.
424   Furthermore, we opted to not include the tracking of the net MTP moments, as we were not
425   confident in the values obtained from IDA. We included the minimisation of the control
426   variables introduced due to the use of the implicit differential equations with a very small
427   weighting factor to avoid redundancy in the process of obtaining an optimal solution and to
428   improve convergence. The experimental and simulated variable differences within $J_{tracking}$,
429   except for the anterior-posterior pelvis translation difference, and the time derivatives of the
430   generalised velocities control variables were each normalised by 10% of their respective
431   experimental range from the trial being tracked. . The anterior-posterior pelvis translation
432   difference was normalised by 0.01 m to ensure it was tracked closely, since the range was much
433   greater in comparison to the other kinematic variables. The remaining variables within $J_{control}$
434   were normalised by their respective upper bounds.
435
436   ***Optimal Control Problem Solution Approach***
437   We converted the data-tracking OCPs described in the previous section to discrete nonlinear
438   programming problems (NLPs) using a direct collocation method. A *flipped* Legendre-Gauss-
439   Radau direct collocation method (Garg et al., 2011) was used to discretise the time horizon of the
440   data-tracking simulations across 80 equally spaced mesh intervals, and each mesh interval was
441   further discretised with 4 points. We set the number of mesh intervals based on a previous study
442   that performed tracking simulations of a running stride using a direct collocation method (Lin
443   and Pandy, 2017), and by considering the trade-off between the time taken for an optimal
444   solution to be reached and the influence of discretising the experimental data to be tracked for
445   different numbers of mesh intervals. The state variables were parameterised with third-order
446   Lagrange polynomials within each mesh interval. The control variables were parameterised at
447   the beginning of each mesh interval and assumed to be piecewise constant throughout a mesh
448   interval. The first-order dynamics constraints were enforced at the collocation points, whilst all
449   the equality and inequality path constraints were enforced at the beginning of each mesh interval.
450   We also included continuity constraints for the state variables between the ending and beginning
451   of the mesh intervals.
452
453   Four data-tracking calibration simulations were performed in total. Three of these calibration
454   simulations featured tracking experimental data from the first trial of each of the sprinting phases
455   (early acceleration, mid-acceleration and maximum velocity) independently whilst also
456   determining the foot-ground contact model parameters (individual calibration simulations). In
457   the fourth calibration simulation we tracked the experimental data from the same three trials
458   simultaneously whilst also determining the foot-ground contact model parameters that were
459   common across the trials (simultaneous calibration simulation). A data-tracking validation
460   simulation was also performed, and we tracked the experimental data from the second maximum
461   velocity phase trial whilst using the foot-ground contact model parameters obtained from the
462   simultaneous calibration simulation. We selected to track the experimental data from the second

463   maximum velocity phase trial for the validation simulation to demonstrate the worst-case
464   scenario from a tracking perspective, as we noticed that the largest tracking errors for the
465   calibration simulations were obtained from the first maximum velocity phase trial.
466
467   For each simulation, the initial guess alongside the lower and upper bounds of the state and
468   control variables were set using the experimental data of the trial being tracked where possible.
469   The generalised coordinates and velocities state variables, and the time derivatives of the
470   generalised velocities control variables were initialised using the splined experimental
471   kinematics. The initial guess for the upper-limb joint actuators control variables was set using the
472   results from IDA. The reserve actuators and GRF control variables were initialised as zero for all
473   the simulations. We used the same initial guess as Falisse et al. (2019a) for the activations and
474   normalised tendon forces state variables, and the derivatives of the activations and normalised
475   tendon forces control variables for all the simulations. The stiffness and damping parameters for
476   the initial guess were set to 1e6 N/m^2 and 0.5 s/m, respectively, while the contact sphere position
477   parameters were initialised so that they cover a plausible region of foot-ground contact during
478   sprinting.
479
480   The lower and upper bounds of the state and control variables pertaining to the skeletal dynamics
481   were set to be 25% less than and more than the minimum and maximum values, respectively,
482   obtained from the experimental data. We set the lower and upper bounds of the variables
483   pertaining to contraction and activation dynamics in accordance with those used by Falisse et al.
484   (2019a). The bounds of the anterior-posterior and medial-lateral positions of the contact sphere
485   parameters were set as to prevent the centres of the spheres from overlapping and to lie within
486   the boundaries of the rearfoot and forefoot segments. The upper bounds of the vertical positions
487   of the contact sphere parameters were set to be the origin of the rearfoot and forefoot segments,
488   whilst the lower bounds of those parameters were set by accounting for length of the spikes
489   attached to athlete's sprinting spikes, the sole height of the sprinting spikes and the behaviour of
490   the compliant foot-ground contact model. The lower and upper bounds of the stiffness and
491   damping parameters were set in line with those reported by previous studies using similar foot-
492   ground contact models (Falisse et al., 2019a; Lin and Pandy, 2017; Porsa et al., 2016; Serrancolí
493   et al., 2019).
494
495   The data-tracking simulations were formulated in MATLAB (2016b, MathWorks Inc., Natick,
496   MA, USA) using CasADi (Andersson et al., 2019), and solved using IPOPT (Wächter and
497   Biegler, 2006) with an adaptive barrier parameter strategy and NLP convergence tolerance of
498   10^{-4}. For each NLP, the variables were scaled to lie on the interval [-1,1] and we also scaled the
499   constraints following the recommendations made by Betts (2010) to improve the convergence
500   rate and numerical conditioning. As an example, the equality path constraints of the pelvis
501   residual forces were scaled by the athlete's bodyweight (BW), thus the largest permissible
502   violation for these constraints was 0.0071 N given our NLP convergence criteria. To further

503   increase the computational efficiency of our simulations we used modified versions of OpenSim
504   and Simbody (Falisse et al., 2019a) for the purposes of evaluating the skeletal dynamic
505   equations. These versions are interfaced with CasADi, which permits the calculation of
506   derivatives using algorithmic differentiation. To evaluate the data-tracking simulations we
507   calculated the root mean squared difference (RMSD) between the tracked experimental and
508   simulated data. For each of the RMSDs reported below we calculated the average RMSD for
509   categories of variables (e.g., global pelvis angles and net lower-limb joint moments), and for the
510   calibration simulations those categorical RMSDs were averaged across the three trials. The GRF
511   RMSD components were expressed relative to the athlete's BW and as a percentage relative to
512   the maximum absolute value of the GRF component obtained experimentally for the trial being
513   tracked. As a further means of evaluating the data-tracking simulations, the filtered EMGs were
514   compared to the corresponding simulated activations.
515

516   **Results**
517   The kinematics and GRF obtained from all the data-tracking simulations were a close match with
518   the experimental kinematics (Figs. 3, 4 and 5) and GRF (Figs. 6 and 7). For both sets of
519   calibration simulations, the average RMSDs were less than 1° and 0.2 cm for the global pelvis
520   angles and translations, respectively, and 1° for the relative joint angles (Table 1). Right ankle
521   plantarflexion-dorsiflexion tended to exhibit the largest RMSD across each of the three trials and
522   for both sets of calibration simulations (4.0° largest RMSD). For the validation simulation, the
523   average RMSDs were less than 1° and 0.3 cm for the global pelvis angles and translations,
524   respectively, and 1° for the relative joint angles. The largest kinematics tracking error for the
525   validation simulation was also obtained for right ankle plantarflexion-dorsiflexion (5.5° RMSD).
526

527   *[Place Figure 3 about here]*
528   **Figure 3. Subset of right lower-limb joint angles for the first early acceleration (A-D), mid-acceleration (E-H) and**
529   **maximum velocity (I-L) phase trials.**
530   *Experimental joint angles are denoted by solid red lines. Simulated joint angles from the individual and simultaneous*
531   *calibration simulations are denoted by dashed blue and green lines, respectively.*
532

533   *[Place Figure 4 about here]*
534   **Figure 4. Subset of global pelvis angles and translations for the first early acceleration (A-D), mid-acceleration (E-**
535   **H) and maximum velocity (I-L) phase trials.**
536   *Experimental global pelvis angles and translations are denoted by solid red lines. Simulated global pelvis angles and*
537   *translations from the individual and simultaneous calibration simulations are denoted by dashed blue and green lines,*
538   *respectively.*
539

540   *[Place Figure 5 about here]*
541   **Figure 5. Subset of right lower-limb joint angles (A-D), and global pelvis angles and translations (E-H) for the**
542   **second maximum velocity phase trial.**
543   *Experimental joint angles, and global pelvis angles and translations are denoted by solid red lines. Simulated joint angles,*
544   *and global pelvis angles and translations from the validation simulation are denoted by dashed blue lines.*
545

546   For the GRF components, the average percentage RMSDs for both sets of calibration simulations
547   (individual and simultaneous) were 8.2% and 8.0% (anterior-posterior), 4.2% and 4.1%
548   (vertical), and 4.2% and 4.0% (medial-lateral). There was a noticeable trend for the tracking
549   errors of the GRF components to increase from the early acceleration to the mid-acceleration
550   trials and from the mid-acceleration to maximum velocity trials for both sets of calibration
551   simulations (Table 1). For the validation simulation, the percentage RMSDs of the GRF
552   components were 11.4% (anterior-posterior), 5.9% (vertical) and 7.5% (medial-lateral).
553
554   *[Place Figure 6 about here]*
555   **Figure 6. Normalised GRF components for the first early acceleration (A-C), mid-acceleration (D-F) and maximum**
556   **velocity (G-I) phase trials.**
557   *Experimental GRF components are denoted by solid red lines. Simulated GRF components from the individual and*
558   *simultaneous calibration simulations are denoted by dashed blue and green lines, respectively.*
559
560   *[Place Figure 7 about here]*
561   **Figure 7. Normalised GRF components for the second maximum velocity phase trial (A-C).**
562   *Experimental GRF components are denoted by solid red lines. Simulated GRF components from the validation simulation*
563   *are denoted by dashed blue lines.*
564
565   The patterns of the net joint moments obtained from the individual and simultaneous data-
566   tracking simulations were found to match the patterns of the experimental net joint moments
567   (Figs. 8 and 9), with average RMSDs of 16.9 and 17.2 Nm, respectively. The average RMSDs of
568   the net lower-limb joint moments were 19.5 and 19.9 Nm for the individual and simultaneous
569   calibration simulations, respectively (Table 2). For the validation simulation, the average
570   RMSDs of the net joint moments and the net lower-limb joint moments were 17.7 and 23.6 Nm,
571   respectively. The tracking errors for the validation simulation were lower than the corresponding
572   tracking errors obtained from the individual (24.9 and 28.6 Nm RMSD) and simultaneous (24.9
573   and 28.7 Nm RMSD) calibration simulations of the maximum velocity phase trial. For the
574   calibration simulations, the pattern of the untracked net right MTP plantarflexion-dorsiflexion
575   moment was markedly different around touchdown and mid-stance (18.2 Nm largest RMSD),
576   whilst for the validation simulation it was in closer agreement (8.7 Nm RMSD).
577
578   *[Place Figure 8 about here]*
579   **Figure 8. Subset of right lower-limb net joint moments for the first early acceleration (A-D), mid-acceleration (E-**
580   **H) and maximum velocity (I-L) phase trials.**
581   *Net MTP moments were not tracked. Experimental net joint moments are denoted by solid red lines. Simulated net joint*
582   *moments from the individual and simultaneous calibration simulations are denoted by dashed blue and green lines,*
583   *respectively.*
584
585   *[Place Figure 9 about here]*
586   **Figure 9. Subset of right lower-limb net joint moments for the second maximum velocity phase trial (A-D).**
587   *Net MTP moments were not tracked. Experimental net joint moments are denoted by solid red lines. Simulated net joint*
588   *moments from the validation simulation are denoted by dashed blue lines.*
589

590   **Table 1. The root mean squared difference (RMSD) of the global pelvis translations and angles, subset of lower-**
591   **limb joint angles and normalised GRF components.**
592   *The values presented are from the individual (Indiv) and simultaneous (Simult) calibration simulations of the first early*
593   *acceleration (Early Acc), mid-acceleration (Mid-Acc) and maximum velocity (Max Vel) phase trials, and from the*
594   *validation (Valid) simulation of the second maximum velocity phase trial.*
595   *[Place Table 1 about here]*
596
597   **Table 2. The root mean squared difference (RMSD) of a subset of lower-limb net joint moments.**
598   *Net MTP moments were not tracked. The values presented are from the individual (Indiv) and simultaneous (Simult)*
599   *calibration simulations of the first early acceleration (Early Acc), mid-acceleration (Mid-Acc) and maximum velocity*
600   *(Max Vel) phase trials, and from the validation (Valid) simulation of the second maximum velocity phase trial.*
601   *[Place Table 2 about here]*
602

603   The simulated activations of the GASTM, TFL, VM and SOL for both sets of calibration
604   simulations displayed similarities in terms of magnitude and timing with the corresponding EMG
605   data (Fig. 10). The simulated GMAX and BF activations from both sets of calibration
606   simulations were markedly different with respect to the corresponding EMG data. A noticeable
607   difference during the end of the stance phase and the beginning of the following flight phase was
608   observed between the simulated activations and EMG data of the GMAX, BF and GASTM, in
609   which the simulated activations continued to ramp up or remain constant, whilst the EMG data
610   tended to zero. For the validation simulation, the simulated activations of the BF, GASTM and
611   VM displayed strong similarities with the corresponding EMG data (Fig. 11). The simulated BF
612   and GASTM activations for the validation simulation, as per the calibration simulations,
613   continued to ramp up near the end of the stance phase and the beginning of the following flight
614   phase, whilst the corresponding EMG data tended to zero. The simulated GMAX activation for
615   the validation simulation displayed similarities to the corresponding EMG data, although the
616   magnitude was discernibly different.
617

618   *[Place Figure 10 about here]*
619   **Figure 10. EMGs and simulated activations from the right lower-limb for the first early acceleration (A-F), mid-**
620   **acceleration (G-L) and maximum velocity (M-R) phase trials.**
621   *The TFL EMG during the mid-acceleration and maximum velocity phase trials, and the SOL EMG during the maximum*
622   *velocity phase trial were omitted due to data collection issues. EMGs are denoted by solid red lines. Simulated activations*
623   *from the individual and simultaneous calibration simulations are denoted by dashed blue and green lines, respectively.*
624   *Gluteus maximus – GMAX, biceps femoris – BF, gastrocnemius – GASTM, tensor fasciae latae – TFL, vastus medialis –*
625   *VM, soleus – SOL.*
626   *[Place Figure 11 about here]*
627   **Figure 11. EMGs and simulated activations from the right lower-limb for the second maximum velocity phase trial**
628   **(A-F).**
629   *The TFL and SOL EMGs were omitted due to data collection issues. EMGs are denoted by solid red lines. Simulated*
630   *activations from the validation simulation are denoted by dashed lines. Gluteus maximus – GMAX, biceps femoris – BF,*
631   *gastrocnemius – GASTM, tensor fasciae latae – TFL, vastus medialis – VM, soleus – SOL.*
632

633   The optimised sphere position parameters were for the most part reasonably similar when
634   obtained from the individual and simultaneous calibration simulations (Table 3 and Fig. 12). The

635   optimised stiffness parameters displayed a trend of increasing from the early acceleration phase
636   trial to the maximum velocity phase trial when determined from the individual calibration
637   simulations. For the simultaneous calibration simulation, the optimised stiffness parameter, was
638   similar to the average value determined from the individual calibration simulations. The
639   optimised damping parameters were found to change minimally between the individual and
640   simultaneous calibration simulations.
641
642   **Table 3. Optimised foot-ground contact model parameters determined from the individual and simultaneous**
643   **calibration simulations.**
644   *Contact spheres s_1 and s_2 were attached to the forefoot segment, the rest were attached to the rearfoot segment. The x, y*
645   *and z subscripts for the contact spheres correspond to the anterior-posterior, vertical and medial-lateral axes of the*
646   *segments to which the spheres were attached.*
647   *[Place Table 3 about here]*
648
649   *[Place Figure 12 about here]*
650   **Figure 12. Optimised contact sphere locations determined from the individual and simultaneous data-tracking**
651   **calibration simulations.**
652   *Sagittal and transverse plane views of the optimised contact sphere locations from the first individual early acceleration*
653   *phase trial (A-B), mid-acceleration phase trial (C-D), maximum velocity phase trial (E-F) calibration simulations, and for*
654   *the three simultaneous trials calibration simulation (G-H). Contact sphere numbers, and rearfoot and forefoot segment*
655   *axes (I-J) have been included to aid with the interpretation of the optimised locations presented in Table 3 (red axis:*
656   *anterior-posterior (x), yellow axis: vertical (y) and green axis: medial-lateral (z)).*
657

Discussion

659   The primary aims of the current study were to develop a musculoskeletal modelling and
660   simulation framework for sprinting, and to evaluate its capability of reproducing highly dynamic
661   experimental data. The secondary aims of this study were to generate dynamically consistent
662   simulated outputs and to identify foot-ground contact model parameters for subsequent
663   predictive simulations. To achieve our aims, we performed a series of data-tracking calibration
664   and validation simulations, based upon a direct collocation optimal control approach. The data-
665   tracking calibration simulations also enabled the determination of the foot-ground contact model
666   parameters from tracking either an individual trial or multiple trials simultaneously. We found
667   that the outputs from the calibration and validation simulations closely matched the experimental
668   data, and this provides confidence in using the framework to address applied sprinting research
669   questions. Importantly, all the simulated outputs were dynamically consistent, implying that no
670   fictious residual forces and moments were necessary to satisfy the dynamics equations of our
671   musculoskeletal model. The proposed framework also includes a novel contribution to the
672   biomechanics modelling and simulation literature, as it enables dynamically consistent
673   simulations of an explosive locomotor task to be performed (with the aerodynamic drag force
674   included), whilst also identifying foot-ground contact model parameters. Furthermore, the
675   simultaneous data-tracking calibration simulation enabled the foot-ground contact model
676   parameters to be determined from multiple trials, which is key to avoid overfit bias.
677

678   The smooth foot-ground contact model used within our framework has been previously shown to
679   be appropriate for reproducing the GRF within walking (Falisse et al., 2019a) and a sit-to-stand
680   task (Serrancolí et al., 2019). In this study, we showed for the first time that the smooth foot-
681   ground contact model permits accurate reproduction of the GRF from different sprinting phases.
682   Average RMSDs of less than 0.07, 0.15 and 0.01 BW for the anterior-posterior, vertical and
683   medial-lateral GRF components, respectively, across all the simulations performed are
684   comparable with another study (Lin and Pandy, 2017), in which similar methods were used to
685   perform dynamically consistent data-tracking simulations of running. In our study we also
686   observed that the GRF tracking errors were the highest for the maximum velocity phase trials,
687   which is likely due to the rapid change in GRF dynamics in comparison to the early acceleration
688   phase trial. This result has also been observed by Lin and Pandy (2017), who reported lower
689   GRF tracking error in walking compared to running trials. Additionally, the simulated GRFs we
690   obtained were noticeably smoother than those obtained by Lin and Pandy (2017), which
691   exhibited unrealistic transients. This can potentially be attributed to the generic foot-ground
692   contact model parameters used in that study, whilst in the current study those parameters were
693   determined from the data-tracking calibration simulations. This study therefore adds to the
694   existing literature which has demonstrated that the determination of the foot-ground contact
695   model parameters via data-tracking simulations enables realistic GRF to be obtained (Falisse et
696   al., 2019a; Serrancolí et al., 2019).
697
698   The ability to track several different trials simultaneously permits a model's parameters to be
699   obtained with the confidence that they are less likely to suffer from overfitting. We observed that
700   the individual data-tracking calibration simulations resulted in only minor improvements in
701   terms of GRF tracking error when compared to those obtained from the simultaneous data-
702   tracking calibration simulation, thus demonstrating the foot-ground contact model's ability to
703   generalise across different sprinting phases. As a means of further evaluating our framework, we
704   performed a data-tracking validation simulation using the foot-ground contact model parameters
705   obtained from the simultaneous data-tracking calibration simulation. The low GRF tracking
706   errors shown in the simultaneous calibration and validation simulations provide confidence in
707   using the foot-ground contact model parameters obtained from the simultaneous data-tracking
708   calibration simulation to perform future predictive simulations of sprinting. It is also worth
709   highlighting that the formulation of a simultaneous data-tracking calibration simulation is greatly
710   facilitated by the direct collocation method and requires minimal adjustments to the NLP
711   problem formulation of tracking a single trial (increase in the number of variables and
712   constraints). Future studies should therefore consider using a similar approach for circumstances
713   in which the parameters cannot be easily obtained empirically.
714
715   From a kinematics perspective, the magnitude of the tracking errors across all simulations are in
716   line with the study by Lin and Pandy (2017), who reported RMSDs of less than 1.5° and 0.6 cm
717   for rotational and translational tracked kinematics during running, respectively. In general, the
718   patterns of simulated kinematics we obtained are in agreement with previous experimental

719 sprinting kinematics (Lai, 2015; von Lieres und Wilkau, 2017), and the kinematics errors we
720 observe are in the same order of magnitude of the experimental error related to human motion
721 capture measurement (Alenezi et al., 2016).We therefore believe that the current framework is of
722 a sufficient accuracy to warrant its use within applied sprinting settings. An aspect of our
723 framework which possibly warrants further improvement is the tracking of right ankle
724 plantarflexion-dorsiflexion, for which the maximum RMSD was 5.5° and it was obtained from
725 the data-tracking validation simulation. We were surprised by this result, as we anticipated the
726 kinematics tracking errors from the validation simulation to be more evenly distributed amongst
727 all the DOFs and higher than those obtained from the equivalent sprinting phase trial of the
728 calibration simulations. In any case, it is worthwhile noting that the smallest detectable
729 difference for peak ankle dorsiflexion during the stance phase of running and bend sprinting is in
730 excess of 10° (Alenezi et al., 2016; Judson et al., 2020), and the largest right ankle dorsiflexion
731 difference we obtained during the stance phase of the validation simulation was 8.9°. Interpreting
732 these findings together suggests that the right ankle kinematics tracking error obtained is likely
733 within the bounds of biological variation and measurement error.

734

735 A wide range of values for the lower-limb net joint moments have been reported within the
736 sprinting literature. For example, the peak net hip flexion-extension moment has been reported to
737 range between ~180 and ~750 Nm during maximum velocity sprinting (Bezodis et al., 2008;
738 Schache et al., 2019), whilst in the current study the peak value was ~400 Nm. While it is
739 possible that these differences may be attributed to an individual athlete's characteristics (e.g.,
740 individual strength differences and anthropometrics) or differences in performance levels, they
741 are also likely to be influenced by the experimental data processing methods and modelling
742 assumptions applied to determine the net joint moments. We therefore opted to track the net joint
743 moments with a lower weighting compared to the kinematics and GRF, which were considered
744 as the most reliable data to track, due to the various uncertainties known to influence the
745 calculation of net joint moments from an IDA (Derrick et al., 2020). Despite the choice to lower
746 the weight of the net joint moments tracking term, we obtained simulated net joint moments that
747 largely followed the general patterns of the net joint moments we determined from IDA and of
748 those reported within the existing sprinting IDA literature (Bezodis et al., 2008; Schache et al.,
749 2019). We would also like to emphasise that the simulated net joint moments we obtained were
750 from dynamically consistent simulations, and they were potentially more physiologically
751 plausible due to the use of Hill-type MTUs.

752

753 In our data-tracking simulations we avoided tracking the net MTP moments, as we felt that the
754 right net MTP moment was unreliable due to the difficulty to distribute the GRF between the
755 rearfoot and forefoot segments. We believed that the right net MTP moments obtained from all
756 the data-tracking simulations were more physiologically plausible and realistic in comparison to
757 those obtained from IDA, which exhibited fluctuations during the first early acceleration and
758 maximum velocity phase trials. Despite the challenges with calculating the net MTP moment
759 from IDA, the MTP has been previously shown to undergo a substantial range of motion during

760   the contact phase of sprinting (Smith et al., 2014). We therefore included a forefoot segment
761   within our model to permit MTP motion. To date, most modelling and simulation studies have
762   chosen to exclude modelling MTP motion, particularly those in which the model's lower-limbs
763   are actuated by Hill-type MTUs (Dorn et al., 2012; Lai et al., 2016). It is not necessarily
764   surprising that previous studies have neglected modelling MTP motion during sprinting, as
765   existing off the shelf musculoskeletal models, similar to the one we used, do not have the
766   capacity to produce MTP moments that are in a similar magnitude to those obtained from
767   isometric dynamometry testing (Goldmann et al., 2013). In our study, we set the upper limit of
768   the MTP reserve actuators to 40 Nm, such that together with the Hill-type MTUs contained
769   within the original model, they were able to better reflect the moment capacity at the MTP DOFs
770   in relation to the existing literature. Future studies should consider exploring how to better model
771   the MTP moment generating components to minimise the reserve actuator reliance.
772
773   An encouraging aspect our study was the similarities between the EMGs and the corresponding
774   simulated activations. We were surprised by the similarities obtained considering the cost
775   function used to resolve the MTU force-sharing problem, minimisation of weighted squared
776   activations, not capturing the time-dependent performance criteria of sprinting. Discrepancies
777   were observed during the end of the stance phase and the beginning of the following flight phase
778   between the simulated activations and EMGs of the BF and GASTM across all the simulations
779   performed. The calibration of the MTU parameters by performing data-tracking simulations
780   and/or the tracking of the EMGs may lead to removing the anomalous simulated activations not
781   observed in the EMGs. The direct collocation optimal control approach we have used in this
782   study also enables the MTU force-sharing problem to be resolved using a cost function that more
783   closely captures the time-dependent performance criteria of sprinting, such as MTU power
784   (Cavagna et al., 1971), and this may also reduce the aforementioned discrepancies.
785
786   The major benefit of the modelling and simulation approach used in this study is that it permits
787   dynamically consistent simulations to be obtained. It is not uncommon to obtain large dynamic
788   inconsistencies in the form of pelvis residual forces and moments that surpass 1000 N and 300
789   Nm, respectively, when performing a standard IDA within sprinting (Aeles et al., 2018). The
790   approach we have used in this study builds on work of other studies (Lin and Pandy, 2017;
791   Pallarès-López et al., 2019) who demonstrated the ability of the direct collocation optimal
792   control approach to reduce residuals within sporting tasks (hopping and running). In this study
793   we demonstrated that it is possible to use this approach to generate dynamically consistent
794   motions in a demanding task that spanned all three planes of motion. Consequently, we
795   recommend that researchers within the sports biomechanics community adopt the approach we
796   have used to increase the fidelity of their results and obtain dynamically consistent motions. A
797   limitation of our study is that we used a generic linearly scaled model. We suspect that the use of
798   a subject-specific model would lead to reduced residuals when performing a standard IDA, due
799   to the model having more representative inertial properties and mass distribution, and we expect

800   that this would improve the tracking of the experimental data due to not needing to overcome the
801   sizeable residuals obtained when using a linearly scaled generic model.
802
803   An alternative approach to generating motions that are closer to being dynamically consistent is
804   RRA, which is included within OpenSim (Delp et al., 2007). RRA is based on using a multibody
805   model actuated by a combination of joint and residual actuators, with the objective to track
806   experimental kinematics whilst also minimising the use of the actuators. The reserve actuators
807   are weighted heavily in comparison to the joint actuators such that the new motion obtained is
808   closer to being dynamically consistent. A beneficial feature of RRA is that it provides
809   recommendations for minimally adjusting the mass properties of the model, and this is a useful
810   feature in circumstances when there are discrepancies between the model's and subject's mass
811   distribution. RRA can then be performed again with the model in which the adjustments to the
812   mass properties have been applied to further refine the dynamic consistency. A similar feature
813   could also be incorporated within the data-tracking optimal control approach used in this study,
814   similarly to how the foot-ground contact model parameters were determined. The downsides of
815   RRA are that it must be performed iteratively to obtain a worthwhile dynamically consistent
816   motion and that it necessitates explicit forward integration to satisfy the dynamics, which can be
817   affected by integration errors. In contrast, the direct collocation optimal control approach used in
818   this study needs only to be performed once to obtain a dynamically consistent solution, and it
819   imposes the dynamics for each time step simultaneously as the state variables are treated as
820   design variables alongside the control variables.
821
822   The most challenging elements to simulate were the transitions between touchdown and take-off.
823   For all the data-tracking simulations performed, we observed discrepancies between the
824   simulated and experimental right lower-limb kinematics and GRF around touchdown and take-
825   off, and these discrepancies were most pronounced for the tracked maximum velocity phase
826   trials (Figs. 6 and 7). Noticeable differences in either knee flexion-extension or ankle
827   plantarflexion-dorsiflexion were accompanied by a mismatch in GRF production timings (largest
828   touchdown and take-off mismatches were 8.0 and 12.6 ms, respectively). More specifically, the
829   right lower-limb appeared to extend earlier and further in the simulations in comparison to the
830   experimental kinematics. This can be explained by the model attempting to position the foot
831   closer to the ground to allow the foot-ground contact model, which is driven by the kinematics,
832   to generate the matching GRF. Future work exploring the geometry of the foot-ground contact
833   model, similar to Ezati et al. (2020), is possibly needed to improve the timing of GRF
834   production.
835
836   Another explanation for the GRF timing differences may concern the filtering we used to process
837   the experimental GRF. We opted to filter both the experimental kinematics and GRF with the
838   same cut-off frequency as per the current recommendations (Derrick et al., 2020). This was to
839   avoid tracking oscillatory net joint moments, which cannot be produced by muscles as they are
840   unable to activate/deactivate instantaneously. However, in this approach the cut-off frequency to

841 filter the GRF is too low based on a residual analysis, which leads to artificially extending the
842 ground contact phase (Mai and Willwacher, 2019; Robertson and Dowling, 2003). Thus, the
843 GRF onset/offset timing differences, in addition to the right lower-limb extension, can
844 potentially be explained by the tracking of the filtered GRF. In fact, the kinematics during the
845 contact phases are tracked closely, particularly for the calibration simulations, which supports
846 this explanation. A further possibility to improve the GRF timings involves filtering the
847 experimental data using matching time varying cut-off frequencies established from the
848 kinematics data (Davis and Challis, 2020), in an attempt to limit the onset/offset discrepancies
849 between the filtered and raw experimental GRF data. It is important to note that filtering the
850 kinematics and GRF data with matching time-varying frequencies may also lead to oscillatory
851 net joint moments when performing a standard IDA, although this has yet to be explored.
852

853 **Conclusions**
854 In conclusion, we have developed a musculoskeletal modelling and simulation framework for
855 sprinting, which is a highly dynamic locomotor task, using an optimal control theory approach.
856 We quantitatively evaluated the framework's ability to reproduce experimental data, which is a
857 first step that is typically ignored within the sports biomechanics modelling and simulation
858 community. The results from the evaluation suggest that the framework can reproduce
859 experimental data from several sprinting phases with low tracking errors, such that we can
860 proceed with performing predictive simulations to assess technique modifications in relation to
861 performance. This is also the first study to provide dynamically consistent three-dimensional
862 muscle-driven simulations of sprinting across different phases. Overlaid videos of the
863 experimental and simulated kinematics, in addition to the corresponding data files, can be
864 accessed online at https://doi.org/10.6084/m9.figshare.12656354.
865

866 **Acknowledgements**

867 The authors would like to thank A. Wallbaum, L. Needham, M. Long, O. Okkonen and J.
868 Cowburn for their assistance with data collection.
869

870 **References**

871 Aeles J, Jonkers I, Debaere S, Delecluse C, and Vanwanseele B. 2018. Muscle-tendon unit
872   length changes differ between young and adult sprinters in the first stance phase of sprint
873   running. *Royal Society Open Science* 5:180332.
874 Alenezi F, Herrington L, Jones P, and Jones RL. 2016. How reliable are lower limb
875   biomechanical variables during running and cutting tasks. *Journal of Electromyography*
876   *and Kinesiology* 30:137-142.
877 Andersson JA, Gillis J, Horn G, Rawlings JB, and Diehl M. 2019. CasADi: a software
878   framework for nonlinear optimization and optimal control. *Mathematical Programming*
879   *Computation* 11:1-36.
880 Betts JT. 2010. *Practical methods for optimal control using nonlinear programming*.
881   Philadelphia, PA: SIAM.

882 Bezodis IN, Kerwin DG, and Salo AI. 2008. Lower-limb mechanics during the support phase of
883   maximum-velocity sprint running. *Medicine & Science in Sports & Exercise* 40:707-715.
884   10.1249/MSS.0b013e318162d162

885 Cavagna GA, Komarek L, and Mazzoleni S. 1971. The mechanics of sprinting. *The Journal of
886   Physiology* 217:709-721.

887 Celik H, and Piazza SJ. 2013. Simulation of aperiodic bipedal sprinting. *Journal of
888   Biomechanical Engineering* 135:081008-081001-081008.

889 Colyer SL, Nagahara R, and Salo AIT. 2018. Kinetic demands of sprinting shift across the
890   acceleration phase: novel analysis of entire waveforms. *Scandinavian Journal of
891   Medicine and Science in Sports* 28:1784-1792.

892 Davis DJ, and Challis JH. 2020. Automatic segment filtering procedure for processing non-
893   stationary signals. *Journal of Biomechanics* 101:109619.

894 De Groote F, Kinney AL, Rao AV, and Fregly BJ. 2016. Evaluation of direct collocation optimal
895   control problem formulations for solving the muscle redundancy problem. *Annals of
896   Biomedical Engineering* 44:2922-2936.

897 De Groote F, Pipeleers G, Jonkers I, Demeulenaere B, Patten C, Swevers J, and De Schutter J.
898   2009. A physiology based inverse dynamic analysis of human gait: potential and
899   perspectives. *Computer Methods in Biomechanics and Biomedical Engineering* 12:563-
900   574.

901 De Ruiter CJ, Didden WJM, Jones DA, and De Haan A. 2000. The force-velocity relationship of
902   human adductor pollicis muscle during stretch and the effects of fatigue. *The Journal of
903   Physiology* 526:671-681.

904 Delp SL, Anderson FC, Arnold AS, Loan P, Habib A, Chand JT, Guendelman E, and Thelen
905   DG. 2007. OpenSim: open-source software to create and analyze dynamic simulations of
906   movement. *IEEE Transactions on Biomedical Engineering* 54:1940-1950.

907 Derrick TR, van den Bogert AJ, Cereatti A, Dumas R, Fantozzi S, and Leardini A. 2020. ISB
908   recommendations on the reporting of intersegmental forces and moments during human
909   motion analysis. *Journal of Biomechanics* 99:109533.

910 Dorn TW, Schache AG, and Pandy MG. 2012. Muscular strategy shift in human running:
911   dependence of running speed on hip and ankle muscle performance. *Journal of
912   Experimental Biology* 215:1944-1956.

913 Dorschky E, Krüger D, Kurfess N, Schlarb H, Wartzack S, Eskofier BM, and van den Bogert AJ.
914   2019. Optimal control simulation predicts effects of midsole materials on energy cost of
915   running. *Computer Methods in Biomechanics and Biomedical Engineering* 22:869-879.

916 Erskine RM, Jones DA, Maffulli N, Williams AG, Stewart CE, and Degens H. 2011. What
917   causes in vivo muscle specific tension to increase following resistance training?
918   *Experimental Physiology* 96:145-155.

919 Ezati M, Brown P, Ghannadi B, and McPhee J. 2020. Comparison of direct collocation optimal
920   control to trajectory optimization for parameter identification of an ellipsoidal foot-
921   ground contact model. *Multibody System Dynamics*:1-23.

922 Falisse A, Serrancolí G, Dembia CL, Gillis J, and De Groote F. 2019a. Algorithmic
923   differentiation improves the computational efficiency of OpenSim-based trajectory
924   optimization of human movement. *PLoS ONE* 14. e0217730

925 Falisse A, Serrancolí G, Dembia CL, Gillis J, Jonkers I, and De Groote F. 2019b. Rapid
926   predictive simulations with complex musculoskeletal models suggests that diverse

927   healthy and pathological human gaits can emerge from similar control strategies. *Journal*
928   *of The Royal Society Interface* 16:20190402.
929 Faude O, Koch T, and Meyer T. 2012. Straight sprinting is the most frequent action in goal
930   situations in professional football. *Journal of Sports Sciences* 30:625-631.
931 Garg D, Patterson MA, Francolin C, Darby CL, Huntington GT, Hager WW, and Rao AV. 2011.
932   Direct trajectory optimization and costate estimation of finite-horizon and infinite-
933   horizon optimal control problems using a Radau pseudospectral method. *Computational*
934   *Optimization and Applications* 49:335-358.
935 Gilchrist LA, and Winter DA. 1996. A two-part, viscoelastic foot model for use in gait
936   simulations. *Journal of Biomechanics* 29:795-798.
937 Goldmann JP, Sanno M, Willwacher S, Heinrich K, and Brüggemann GP. 2013. The potential of
938   toe flexor muscles to enhance performance. *Journal of Sports Sciences* 31:424-433.
939 Hamner SR, Seth A, and Delp SL. 2010. Muscle contributions to propulsion and support during
940   running. *Journal of Biomechanics* 43:2709-2716. 10.1016/j.jbiomech.2010.06.025
941 Hermens HJ, Freriks B, Disselhorst-Klug C, and Rau G. 2000. Development of
942   recommendations for SEMG sensors and sensor placement procedures. *Journal of*
943   *Electromyography and Kinesiology* 10:361-374.
944 Hunter JP, Marshall RN, and McNair PJ. 2004. Interaction of step length and step rate during
945   sprint running. *Medicine & Science in Sports & Exercise* 36:261-271.
946 Jansen C, and McPhee J. 2020. Predictive dynamic simulation of Olympic track cycling standing
947   start using direct collocation optimal control. *Multibody System Dynamics*:1-18.
948 Judson LJ, Churchill SM, Barnes A, Stone JA, Brookes IGA, and Wheat J. 2020. Measurement
949   of bend sprinting kinematics with three-dimensional motion capture: a test-retest
950   reliability study. *Sports Biomechanics* 19:761-777.
951 Lai A. 2015. Muscle and tendon mechanical interactions during human locomotion. PhD Thesis.
952   The University of Melbourne.
953 Lai A, Schache AG, Brown NA, and Pandy MG. 2016. Human ankle plantar flexor muscle-
954   tendon mechanics and energetics during maximum acceleration sprinting. *Journal of The*
955   *Royal Society Interface* 13:20160391. 10.1098/rsif.2016.0391
956 Lin YC, and Pandy MG. 2017. Three-dimensional data-tracking dynamic optimization
957   simulations of human locomotion generated by direct collocation. *Journal of*
958   *Biomechanics* 59:1-8.
959 Mai P, and Willwacher S. 2019. Effects of low-pass filter combinations on lower extremity joint
960   moments in distance running. *Journal of Biomechanics* 95:109311.
961 Meyer AJ, Eskinazi I, Jackson JN, Rao AV, Patten C, and Fregly BJ. 2016. Muscle synergies
962   facilitate computational prediction of subject-specific walking motions. *Frontiers in*
963   *Bioengineering and Biotechnology* 4:77.
964 Miller RH, and Hamill J. 2015. Optimal footfall patterns for cost minimization in running.
965   *Journal of Biomechanics* 48:2858-2864.
966 Morin JB, Edouard P, and Samozino P. 2011. Technical ability of force application as a
967   determinant factor of sprint performance. *Medicine & Science in Sports & Exercise*
968   43:1680-1688.
969 Neptune RR. 2000. Computer modeling and simulation of human movement: applications in
970   sport and rehabilitation. *Physical Medicine and Rehabilitation Clinics of North America*
971   11:417-434.

972 Oh K, and Park S. 2017. The bending stiffness of shoes is beneficial to running energetics if it
973   does not disturb the natural MTP joint flexion. *Journal of Biomechanics* 53:127-135.
974 Pallarès-López R, Alvim FC, Febrer-Nafría M, Menegaldo LL, and Font-Llagunes JM. 2019.
975   Assessment of residual reduction procedures for high-speed tasks. *Gait & Posture*
976   73:116-119.
977 Porsa S, Lin YC, and Pandy MG. 2016. Direct methods for predicting movement biomechanics
978   based upon optimal control theory with implementation in OpenSim. *Annals of*
979   *Biomedical Engineering* 44:2542-2557.
980 Quinn MD. 2003. The effects of wind and altitude in the 200-m sprint. *Journal of Applied*
981   *Biomechanics* 19:49-59.
982 Robertson DGE, and Dowling J. 2003. Design and responses of Butterworth and critically
983   damped digital filters. *Journal of Electromyography and Kinesiology* 13:569-573.
984 Salo AIT, Bezodis IN, Batterham AM, and Kerwin DG. 2011. Elite sprinting: are athletes
985   individually step-frequency or step-length reliant? *Medicine & Science in Sports &*
986   *Exercise* 43:1055-1062.
987 Samozino P, Rabita G, Dorel S, Slawinski J, Peyrot N, Saez de Villarreal E, and Morin JB. 2016.
988   A simple method for measuring power, force, velocity properties, and mechanical
989   effectiveness in sprint running. *Scandinavian Journal of Medicine and Science in Sports*
990   26:648-658.
991 Santuz A, Ekizos A, Kunimasa Y, Kijima K, Ishikawa M, and Arampatzis A. 2020. Lower
992   complexity of motor primitives ensures robust control of high-speed human locomotion.
993   *bioRxiv*. 10.1101/2020.04.24.055277
994 Sasaki K, Neptune RR, and Kautz SA. 2009. The relationships between muscle, external,
995   internal and joint mechanical work during normal walking. *Journal of Experimental*
996   *Biology* 212:738-744.
997 Schache AG, Lai AKM, Brown NAT, Crossley KM, and Pandy MG. 2019. Lower-limb joint
998   mechanics during maximum acceleration sprinting. *Journal of Experimental Biology* 222.
999   doi: 10.1242/jeb.209460
1000 Schultz G, and Mombaur K. 2010. Modeling and optimal control of human-like running.
1001   *IEEE/ASME Transactions on Mechatronics* 15:783-792.
1002 Serrancolí G, Falisse A, Dembia CL, Vantilt J, Tanghe K, Lefeber D, Jonkers I, and De Groote
1003   F. 2019. Subject-exoskeleton contact model calibration leads to accurate interaction force
1004   predictions. *IEEE Transactions on Neural Systems and Rehabilitation Engineering*
1005   27:1597-1605.
1006 Sherman MA, Seth A, and Delp SL. 2011. Simbody: multibody dynamics for biomedical
1007   research. *Procedia IUTAM* 2:241-261.
1008 Smith G, Lake M, and Lees A. 2014. Metatarsophalangeal joint function during sprinting: a
1009   comparison of barefoot and sprint spike shod foot conditions. *Journal of Applied*
1010   *Biomechanics* 30:206-212.
1011 Toon D, Kamperman N, Ajoku U, Hopkinson N, and Caine M. 2006. Benchmarking stiffness of
1012   current spring spikes and concept selective laser sintered nylon outsoles. In: Moritz EF,
1013   and Haake S, eds. *The Engineering of Sport 6*. Berlin: Springer-Verlag, 415-420.
1014 Umberger BR, and Miller RH. 2017. Optimal control modeling of human movement. In: Müller
1015   B, Wolf SI, Bruggemann GP, Deng Z, McIntosh A, Miller F, and Selbie WS, eds.
1016   *Handbook of Human Motion*. 1st ed. New York City, USA: Springer International
1017   Publishing.

1018   von Lieres und Wilkau HC. 2017. Understanding biomechanical differences in technique
1019   between phases of a sprint. PhD Thesis. Cardiff Metropolitan University.
1020   Wächter A, and Biegler LT. 2006. On the implementation of an interior-point filter line-search
1021   algorithm for large-scale nonlinear programming. *Mathematical Programming* 106:25-
1022   57.
1023   Winter DA. 2009. *Biomechanics and Motor Control of Human Movement*. Toronto, Canada:
1024   John Wiley & Sons.
1025   Yeadon MR, and Challis JH. 1994. The future of performance-related sports biomechanics
1026   research. *Journal of Sports Sciences* 12:3-32. 10.1080/02640419408732156
1027   Yong JR, Silder A, and Delp SL. 2014. Differences in muscle activity between natural forefoot
1028   and rearfoot strikers during running. *Journal of Biomechanics* 47:3593-3597.
1029   Zajac FE. 1989. Muscle and tendon: propeties, models, scaling, and application to biomechanics
1030   and motor control. *Critical Reviews in Biomedical Engineering* 17:359-411.
1031

Figure 1

Experimental data collection setup (A), and placement of retro-reflective markers, acrylic clusters, and EMG electrodes (B-C).

The force plates setup provided a 4.5 m segment of the track to capture GRF, and this permitted GRF data from a minimum of two successive steps to be captured for each trial. The calibrated motion capture volume covered approximately 9.5 (length) × 1.5 (width) × 2 (height) m^3.

A

B

C

Figure 2

Three-dimensional musculoskeletal model (Hamner et al., 2010) used in the current study.

The same model was used to determine experimental kinematics and kinetics from inverse kinematics and dynamics analyses, respectively, and perform data-tracking simulations. The virtual model markers are denoted by pink spheres.
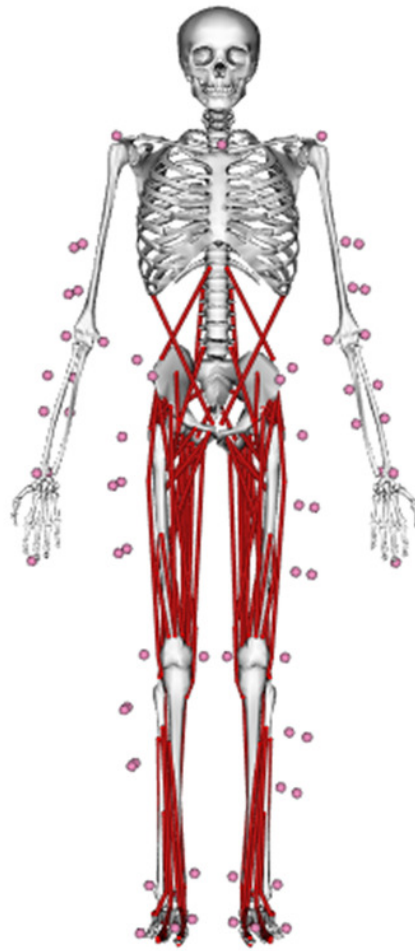
Figure 3

Subset of right lower-limb joint angles for the first early acceleration (A-D), mid-acceleration (E-H) and maximum velocity (I-L) phase trials.

Experimental joint angles are denoted by solid red lines. Simulated joint angles from the individual and simultaneous calibration simulations are denoted by dashed blue and green lines, respectively.
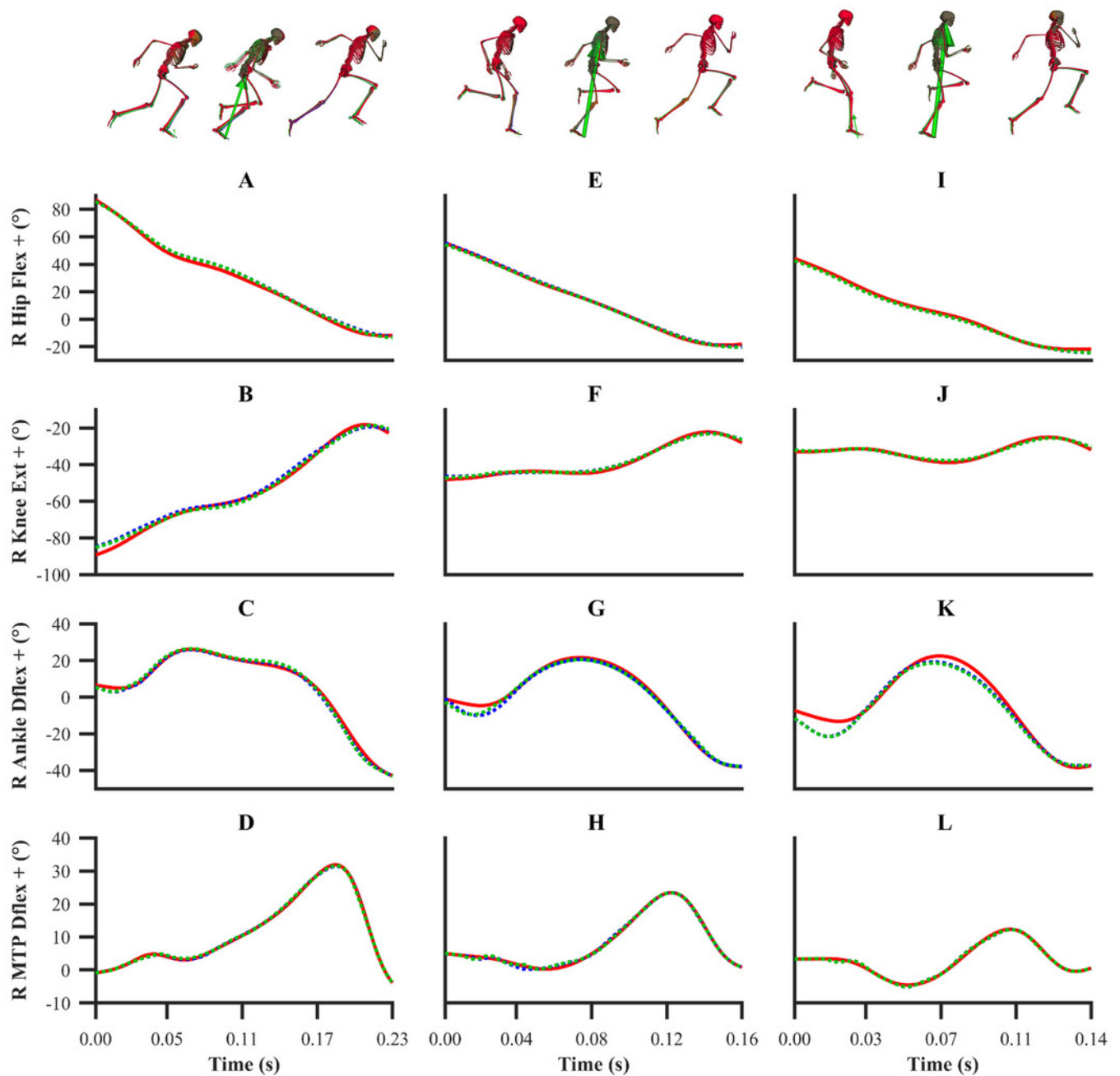
Figure 4

Subset of global pelvis angles and translations for the first early acceleration (A-D), mid-acceleration (E-H) and maximum velocity (I-L) phase trials.

Experimental global pelvis angles and translations are denoted by solid red lines. Simulated global pelvis angles and translations from the individual and simultaneous calibration simulations are denoted by dashed blue and green lines, respectively.
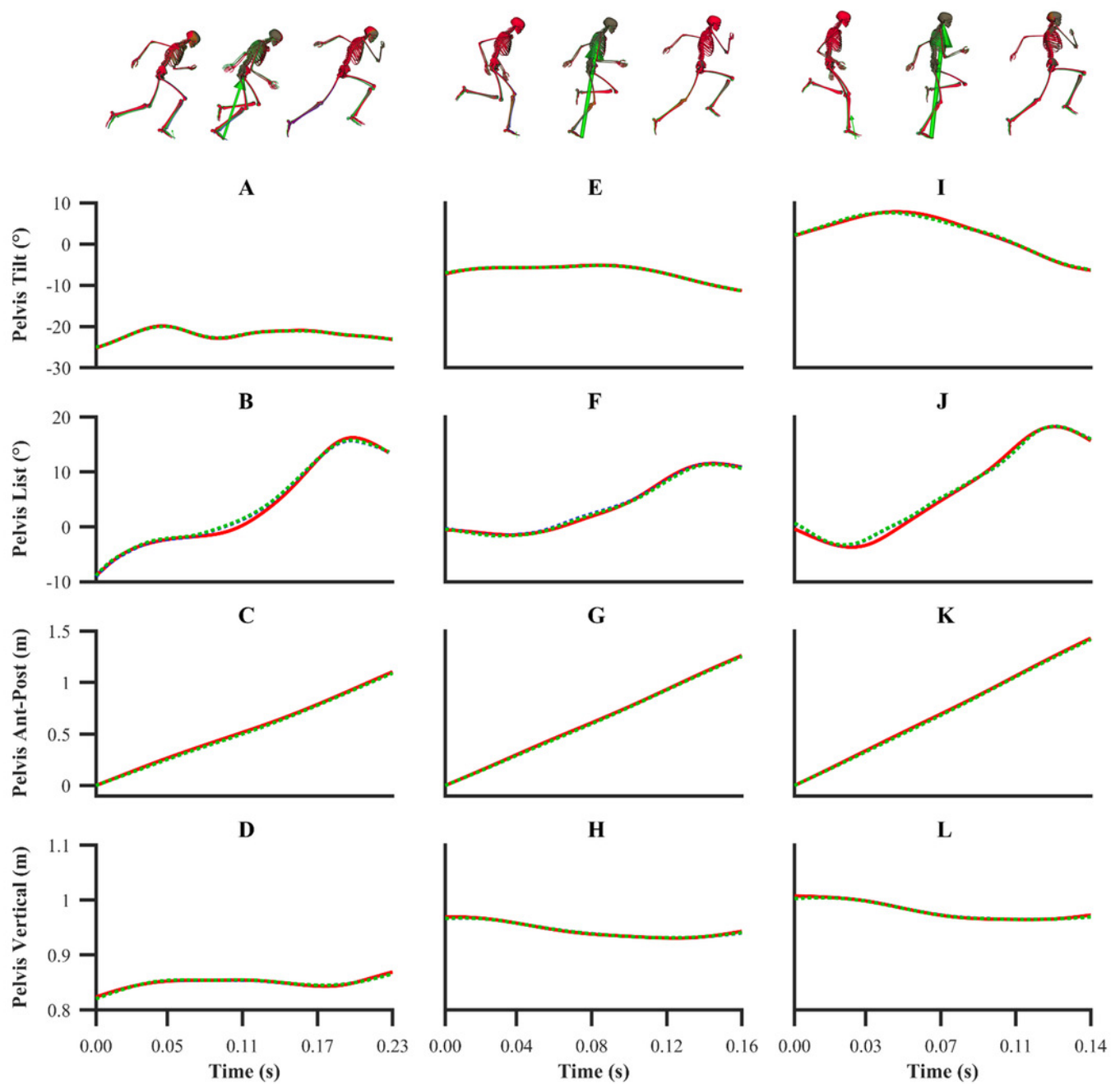
Figure 5

Subset of right lower-limb joint angles (A-D), and global pelvis angles and translations (E-H) for the second maximum velocity phase trial.

Experimental joint angles, and global pelvis angles and translations are denoted by solid red lines. Simulated joint angles, and global pelvis angles and translations from the validation simulation are denoted by dashed blue lines.

A

B

C

D

E

F

G

H
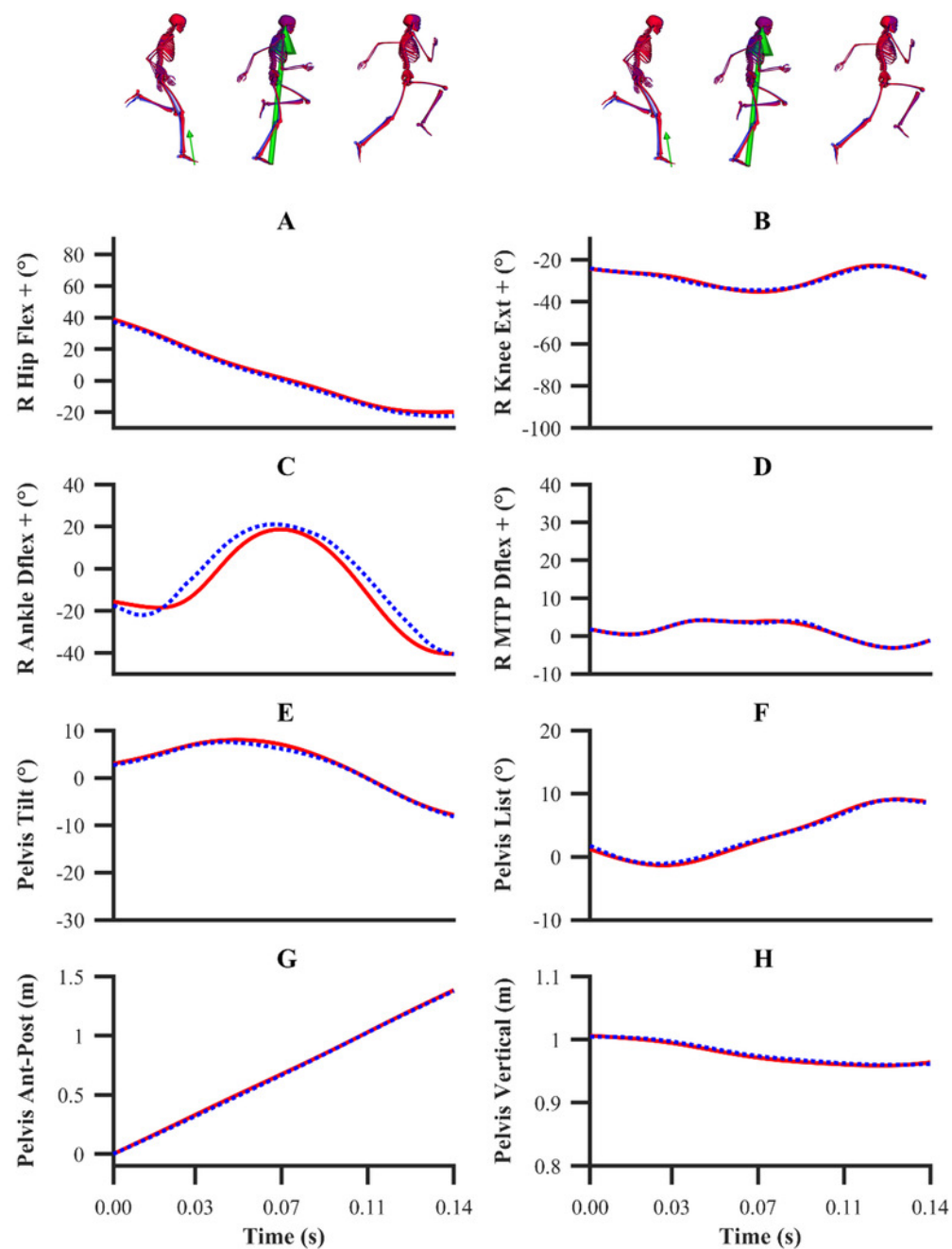
Figure 6

Normalised GRF components for the first early acceleration (A-C), mid-acceleration (D-F) and maximum velocity (G-I) phase trials.

Experimental GRF components are denoted by solid red lines. Simulated GRF components from the individual and simultaneous calibration simulations are denoted by dashed blue and green lines, respectively.
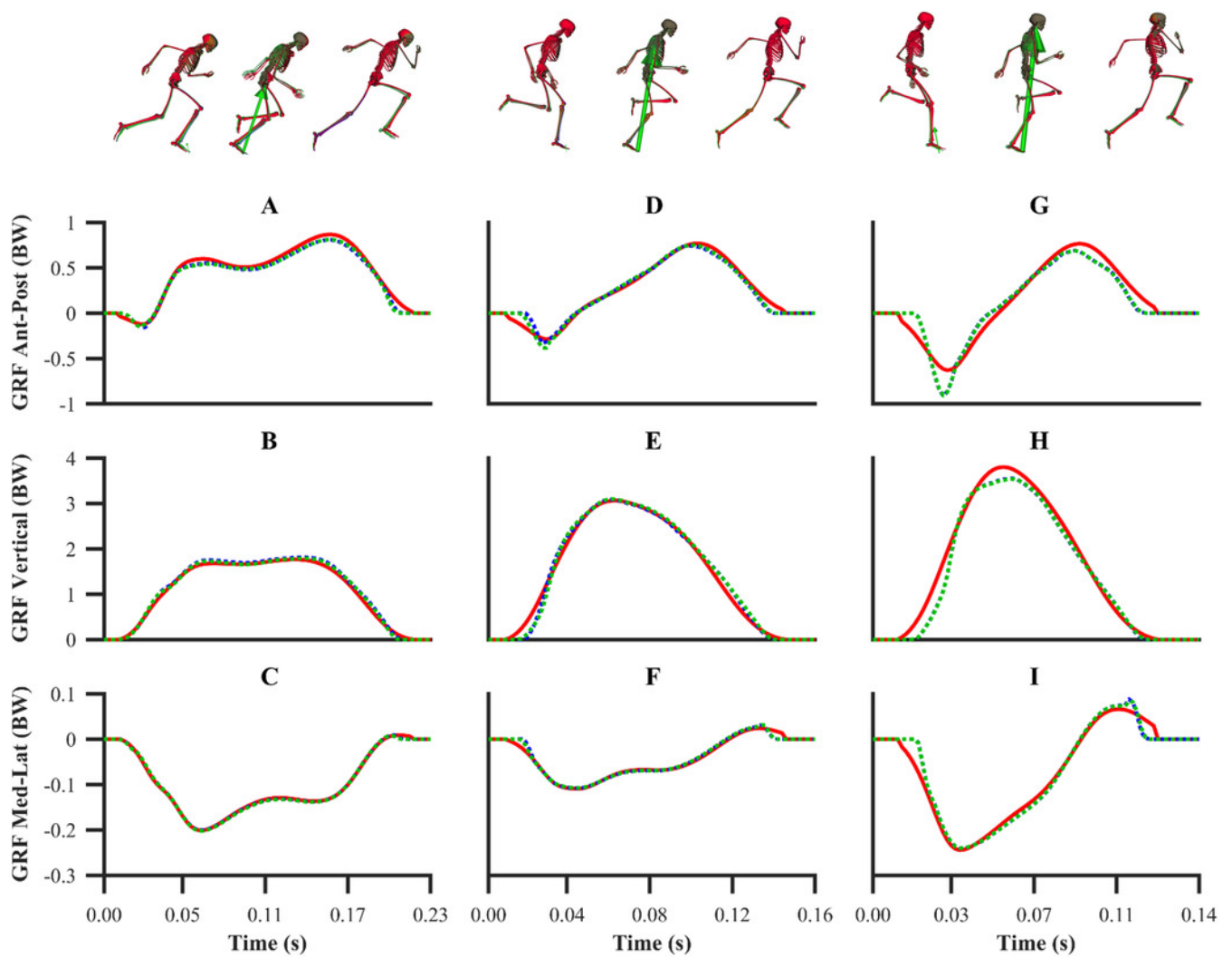
Figure 7

Normalised GRF components for the second maximum velocity phase trial (A-C).

Experimental GRF components are denoted by solid red lines. Simulated GRF components from the validation simulation are denoted by dashed blue lines.
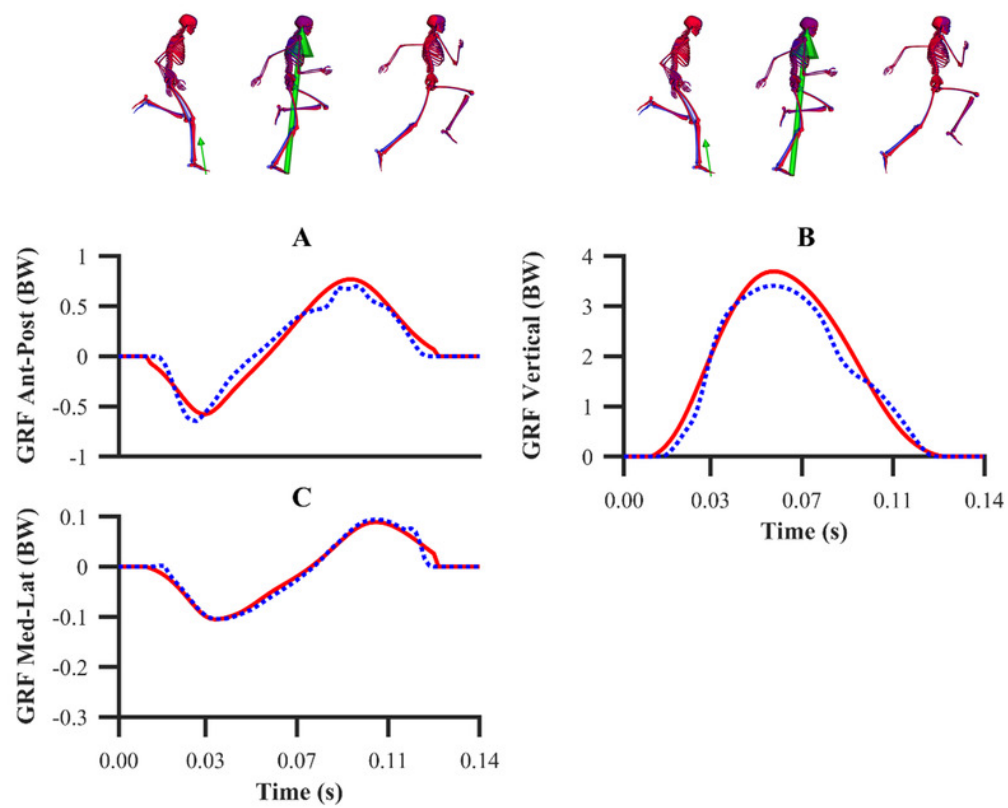
Figure 8

Subset of right lower-limb net joint moments for the first early acceleration (A-D), mid-acceleration (E-H) and maximum velocity (I-L) phase trials.

Net MTP moments were not tracked. Experimental net joint moments are denoted by solid red lines. Simulated net joint moments from the individual and simultaneous calibration simulations are denoted by dashed blue and green lines, respectively.
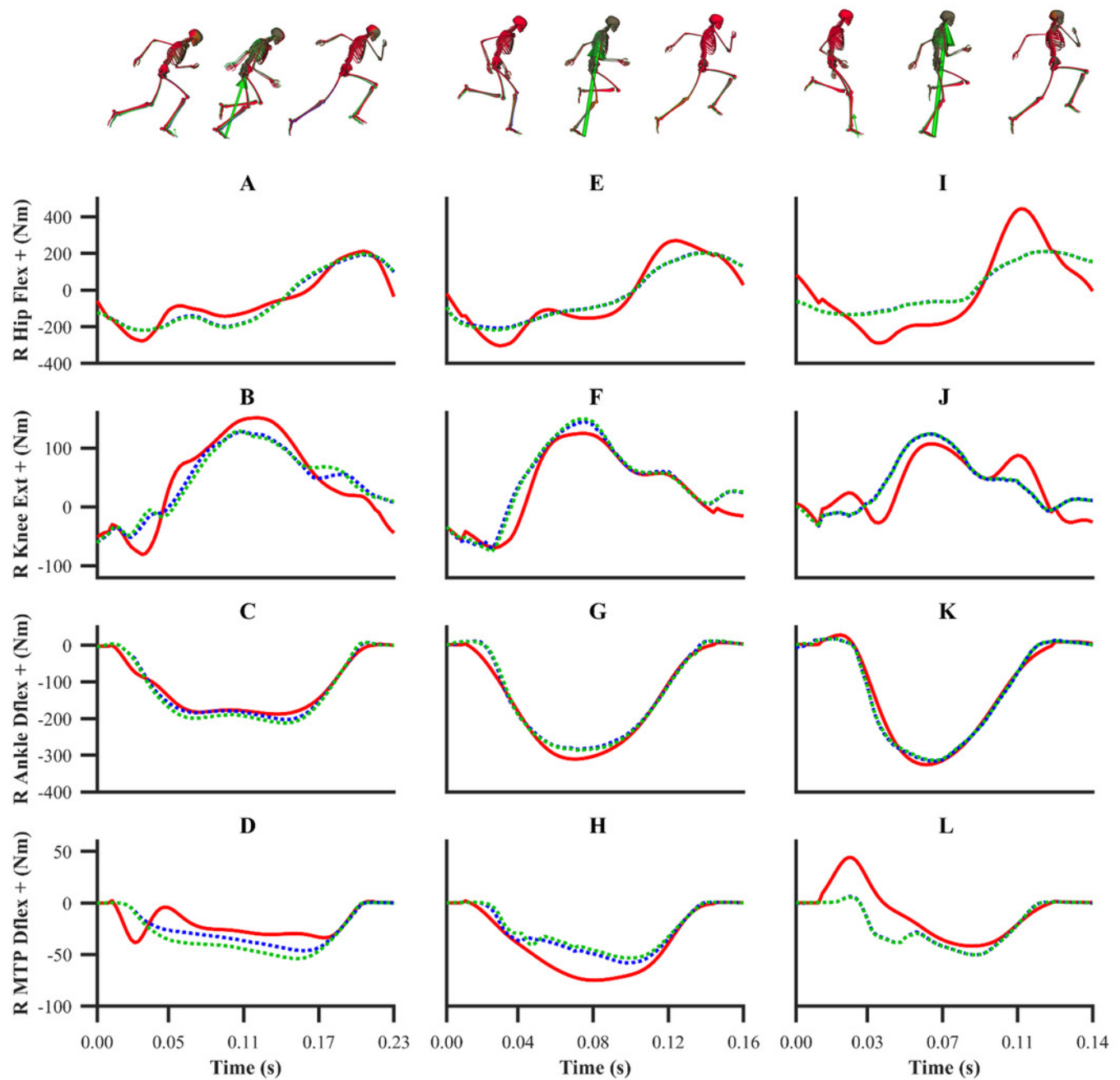
Figure 9

Subset of right lower-limb net joint moments for the second maximum velocity phase trial (A-D).

Net MTP moments were not tracked. Experimental net joint moments are denoted by solid red lines. Simulated net joint moments from the validation simulation are denoted by dashed blue lines.
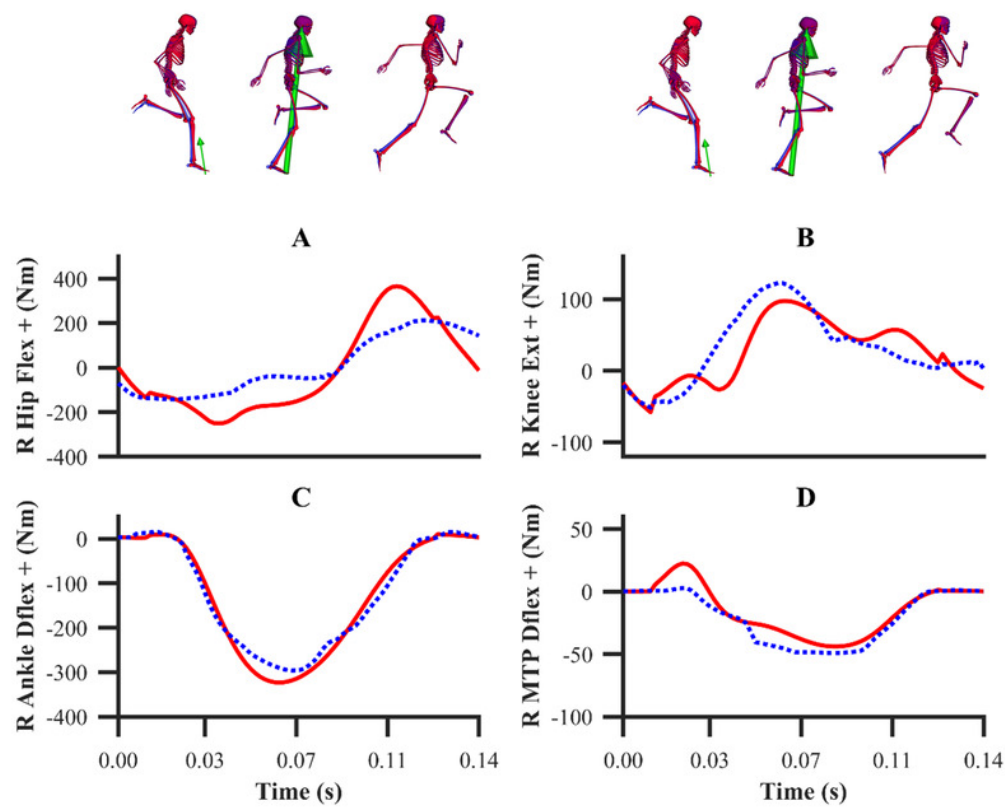
Figure 10

EMGs and simulated activations from the right lower-limb for the first early acceleration (A-F), mid-acceleration (G-L) and maximum velocity (M-R) phase trials.

The TFL EMG during the mid-acceleration and maximum velocity phase trials, and the SOL EMG during the maximum velocity phase trial were omitted due to data collection issues. EMGs are denoted by solid red lines. Simulated activations from the individual and simultaneous calibration simulations are denoted by dashed blue and green lines, respectively. Gluteus maximus – GMAX, biceps femoris – BF, gastrocnemius – GASTM, tensor fasciae latae – TFL, vastus medialis – VM, soleus – SOL.

A

R GMAX
EMG/Act (-)

G

M

B

R BF
EMG/Act (-)

H

N

C

R GASTM
EMG/Act (-)

I

O

D

R TFL
EMG/Act (-)

J

P

E

R VM
EMG/Act (-)

K

Q

F

R SOL
EMG/Act (-)

L

R

Time (s)

Time (s)

Time (s)
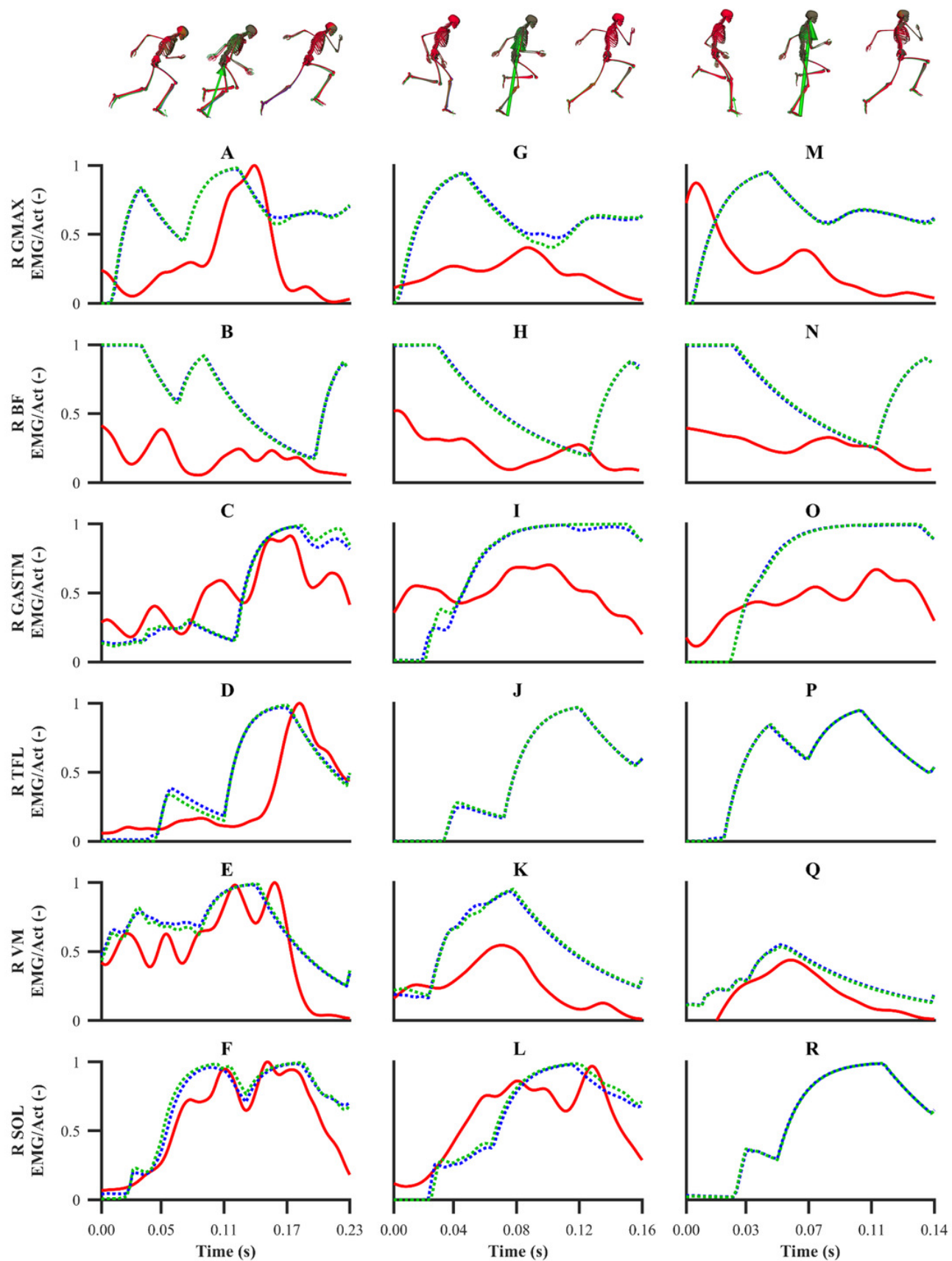
Figure 11

EMGs and simulated activations from the right lower-limb for the second maximum velocity phase trial (A-F).

The TFL and SOL EMGs were omitted due to data collection issues. EMGs are denoted by solid red lines. Simulated activations from the validation simulation are denoted by dashed lines. Gluteus maximus – GMAX, biceps femoris – BF, gastrocnemius – GASTM, tensor fasciae latae – TFL, vastus medialis – VM, soleus – SOL.
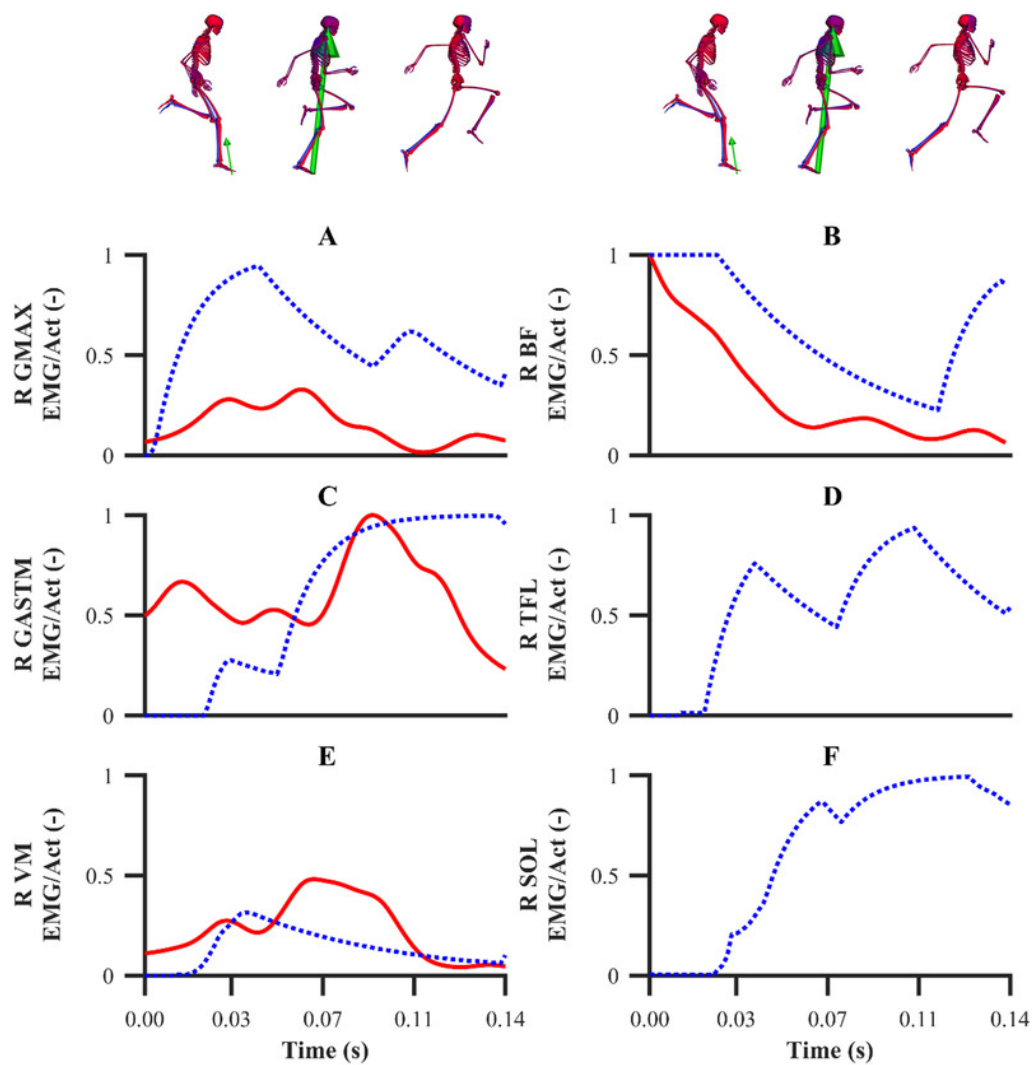
Figure 12

Optimised contact sphere locations determined from the individual and simultaneous data-tracking calibration simulations.

Sagittal and transverse plane views of the optimised contact sphere locations from the first individual early acceleration phase trial (A-B), mid-acceleration phase trial (C-D), maximum velocity phase trial (E-F) calibration simulations, and for the three simultaneous trials calibration simulation (G-H). Contact sphere numbers, and rearfoot and forefoot segment axes (I-J) have been included to aid with the interpretation of the optimised locations presented in Table 3 (red axis: anterior-posterior (x), yellow axis: vertical (y) and green axis: medial-lateral (z)).
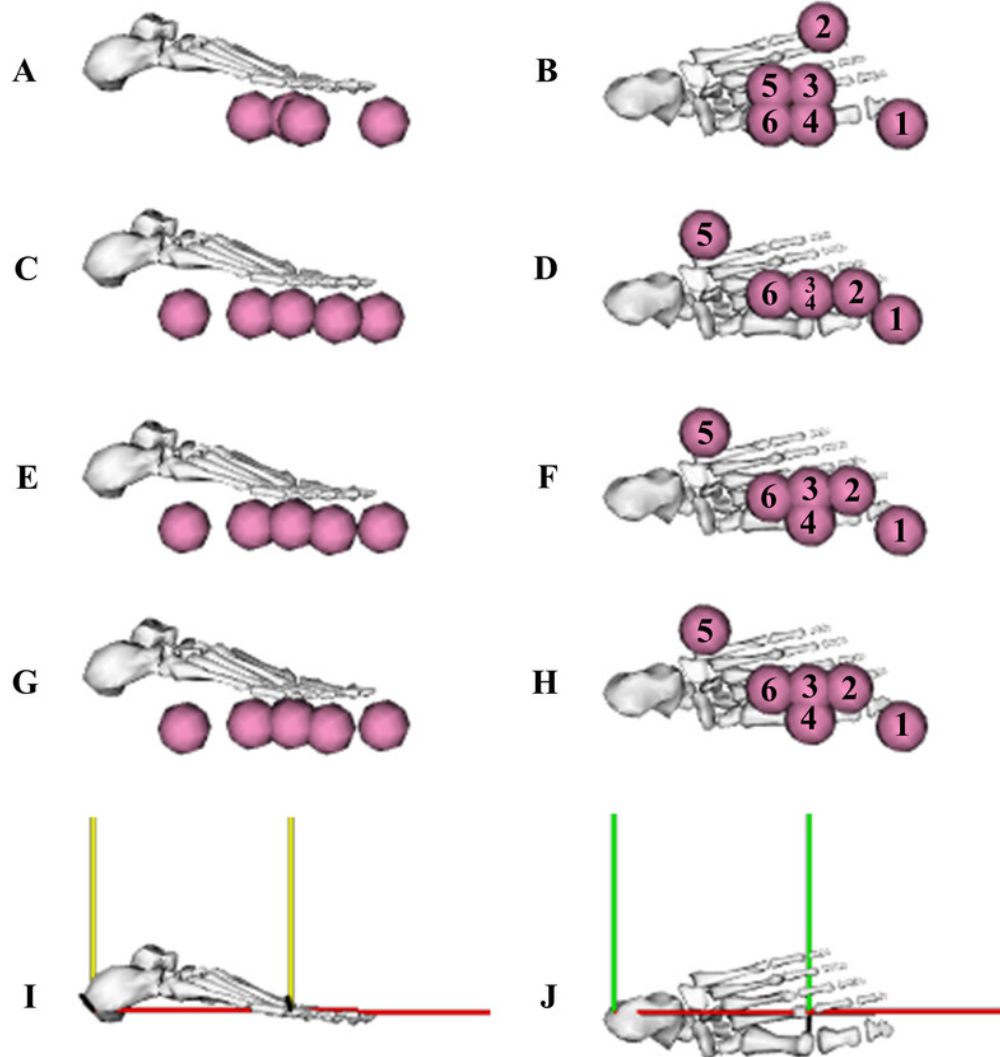
The root mean squared difference (RMSD) of the global pelvis translations and angles, subset of lower-limb joint angles and normalised GRF components.

The values presented are from the individual (Indiv) and simultaneous (Simult) calibration simulations of the first early acceleration (Early Acc), mid-acceleration (Mid-Acc) and maximum velocity (Max Vel) phase trials, and from the validation (Valid) simulation of the second maximum velocity phase trial.

1 **Table 1. The root mean squared difference (RMSD) of the global pelvis translations and angles, subset of lower-**
2 **limb joint angles and normalised GRF components.**
3 *The values presented are from the individual (Indiv) and simultaneous (Simult) calibration simulations of the first early*
4 *acceleration (Early Acc), mid-acceleration (Mid-Acc) and maximum velocity (Max Vel) phase trials, and from the*
5 *validation (Valid) simulation of the second maximum velocity phase trial.*

	Early Acc		Mid-Acc		Max Vel		Max Vel
RMSD	Indiv	Simult	Indiv	Simult	Indiv	Simult	
Pelvis Translations							
Pelvis Ant-Post (cm)	0.4	0.4	0.3	0.3	0.4	0.4	0.4
Pelvis Vertical (cm)	0.1	0.2	0.1	0.1	0.1	0.1	0.2
Pelvis Med-Lat (cm)	0.1	0.1	0.1	0.1	0.1	0.1	0.1
Pelvis Angles							
Pelvis List (°)	0.1	0.1	0.1	0.1	0.3	0.3	0.4
Pelvis Tilt (°)	0.5	0.6	0.2	0.2	0.3	0.3	0.3
Pelvis Rotation (°)	1.0	1.1	0.7	0.7	0.8	0.8	0.6
Lower-limb Joint Angles							
R Hip Flex (°)	1.8	1.7	0.6	0.7	1.3	1.3	1.4
R Knee Ext (°)	2.0	1.6	0.9	0.8	0.6	0.6	0.5
R Ankle Dflex (°)	1.2	1.5	2.0	1.9	3.7	4.0	5.5
R MTP Dflex (°)	0.3	0.3	0.4	0.4	0.3	0.3	0.2
L Hip Flex (°)	2.7	2.7	1.5	1.3	1.4	1.5	2.7
L Knee Ext (°)	0.3	0.4	0.2	0.2	0.6	0.6	1.4
L Ankle Dflex (°)	0.3	0.3	0.2	0.2	0.2	0.2	0.2
L MTP Dflex (°)	1e-2	1e-2	1e-2	1e-2	1e-2	1e-2	1e-2
GRF							
Ant-Post (BW)	0.042	0.045	0.047	0.041	0.103	0.102	0.088
Vertical (BW)	0.058	0.049	0.112	0.122	0.213	0.213	0.219
Med-Lat (BW)	0.002	0.003	0.005	0.005	0.016	0.016	0.008

The root mean squared difference (RMSD) of a subset of lower-limb net joint moments.

Net MTP moments were not tracked. The values presented are from the individual (Indiv) and simultaneous (Simult) calibration simulations of the first early acceleration (Early Acc), mid-acceleration (Mid-Acc) and maximum velocity (Max Vel) phase trials, and from the validation (Valid) simulation of the second maximum velocity phase trial.

1 **Table 2. The root mean squared difference (RMSD) of a subset of lower-limb net joint moments.**
2 *Net MTP moments were not tracked. The values presented are from the individual (Indiv) and simultaneous (Simult)*
3 *calibration simulations of the first early acceleration (Early Acc), mid-acceleration (Mid-Acc) and maximum velocity*
4 *(Max Vel) phase trials, and from the validation (Valid) simulation of the second maximum velocity phase trial.*

	Early Acc		Mid-Acc		Max Vel		Max Vel
RMSD	Indiv	Simult	Indiv	Simult	Indiv	Simult	
Lower-limb Net Joint Moments							
R Hip Flex (Nm)	46.9	49.8	58.2	57.0	124.2	123.5	99.4
R Knee Ext (Nm)	26.1	30.3	21.8	21.4	29.1	28.5	30.2
R Ankle Dflex (Nm)	12.3	18.0	16.9	16.3	14.3	14.1	18.8
R MTP Dflex (Nm)	11.9	16.9	13.6	15.9	18.0	18.2	8.7
L Hip Flex (Nm)	33.7	34.1	25.9	26.5	42.4	44.2	40.5
L Knee Ext (Nm)	6.4	7.1	5.0	4.4	12.7	12.3	16.1
L Ankle Dflex (Nm)	0.5	0.4	0.3	0.3	0.8	0.9	0.7
L MTP Dflex (Nm)	2e-2	2e-2	2e-2	2e-2	5e-2	6e-2	5e-2

Optimised foot-ground contact model parameters determined from the individual and simultaneous data-tracking calibration simulations.

Contact spheres s_1 and s_2 were attached to the forefoot segment, the rest were attached to the rearfoot segment. The x, y and z subscripts for the contact spheres correspond to the anterior-posterior, vertical and medial-lateral axes of the segments to which the spheres were attached to.

1 **Table 3. Optimised foot-ground contact model parameters determined from the individual and simultaneous**
2 **calibration simulations.**
3 *Contact spheres s_1 and s_2 were attached to the forefoot segment, the rest were attached to the rearfoot segment. The x, y*
4 *and z subscripts for the contact spheres correspond to the anterior-posterior, vertical and medial-lateral axes of the*
5 *segments to which the spheres were attached.*

Parameter	Early Acceleration	Mid-Acceleration	Maximum Velocity	Simultaneous
Sphere s_{1x} (m)	0.070	0.066	0.069	0.070
Sphere s_{1y} (m)	-0.030	-0.030	-0.030	-0.030
Sphere s_{1z} (m)	-0.028	-0.020	-0.030	-0.029
Sphere s_{2x} (m)	0.010	0.035	0.031	0.029
Sphere s_{2y} (m)	-0.030	-0.030	-0.030	-0.030
Sphere s_{2z} (m)	0.045	3.07e-7	3.04e-7	1.52e-8
Sphere s_{3x} (m)	0.150	0.150	0.150	0.150
Sphere s_{3y} (m)	-0.028	-0.028	-0.028	-0.028
Sphere s_{3z} (m)	6.46e-6	5.41e-5	1.12e-6	6.88e-8
Sphere s_{4x} (m)	0.150	0.150	0.150	0.150
Sphere s_{4y} (m)	-0.028	-0.028	-0.028	-0.028
Sphere s_{4z} (m)	-0.025	-4.79e-5	-0.022	-0.023
Sphere s_{5x} (m)	0.120	0.070	0.070	0.070
Sphere s_{5y} (m)	-0.028	-0.028	-0.028	-0.028
Sphere s_{5z} (m)	9.70e-6	0.045	0.045	0.045
Sphere s_{6x} (m)	0.120	0.120	0.120	0.120
Sphere s_{6y} (m)	-0.028	-0.028	-0.028	-0.028
Sphere s_{6z} (m)	-0.025	-2.08e-6	-9.32e-6	-6.09e-8
Stiffness (N/m^2)	1.17e6	1.64e6	1.79e6	1.60e6
Damping (s/m)	0.073	0.110	0.063	0.072